Simulating Granular Media on the Computer

H.J. Herrmann

P.M.M.H., (U.R.A. 857), E.S.P.C.I.,
10 rue Vauquelin, 75231 Paris, France

Abstract: Granular materials, like sand or powder, can present very intriguing effects. When shaken, sheared or poured they show segregation, convection and spontaneous fluctuations in densities and stresses. I will discuss the modeling of a granular medium on a computer by simulating a packing of elastic spheres via Molecular Dynamics. Dissipation of energy and shear friction at collisions are included. In the physical range the friction coefficient is found to be a linear function of the angle of repose. On a vibrating plate the formation of convection cells due to walls or amplitude modulations can be observed. The onset of fluidization can be determined and is in good agreement with experiments. Segregation of larger particles is found to be always accompanied by convection cells. There is also ample experimental evidence showing the existence of spontaneous density patterns in granular material flowing through pipes or hoppers. The Molecular Dynamics simulations show that these density fluctuations follow a $1/f^{\alpha}$ spectrum. I compare this behavior to deterministic one-dimensional traffic models. A model with continuous positions and velocities shows self-organized critical jamming behind a slower car. The experimentally observed effects are also reproduced by Lattice Gas and Boltzmann Lattice Models. Density waves are spontaneously generated when the viscosity has a nonlinear dependence on density which characterizes granular flow. We also briefly sketch a thermodynamic formalism for loose granular material. In a dense packing non-linear acoustic phenomena, like the pressure dependence of the sound velocity are studied. Finally the plastic shear bands occurring in large scale deformations of compactified granular media are investigated using an explicit Lagrangian technique.

1. Introduction

Many rather astonishing phenomena are known to occur when granular materials like sand or powders move [1 – 4] Examples are the so-called "Brazil nut" segregation [5 – 8], heap formation under vibration [9 – 11], density waves emitted from outlets [12] and 1/f noise in the power spectra of local forces [13]. All these effects originate in the ability of granular materials to form a hybrid state between a fluid and a solid: When the density exceeds a certain value, the critical dilatancy [14, 15], it is resistant to shear, like solids, while below this density it will "fluidify". This fluidified state can be rather complex, specially in the presence of density fluctuations and density gradients.

Particularly suited to study this fluidization is an experiment where sand is put on a loudspeaker or on a vibrating table [9 – 11, 16, 17]. Under gravity the sand jumps up and down and although kinetic energy is strongly dissipated, collisions among the grains reduce its density thereby allowing it to flow ("fluidization"). Under certain circumstances flow between top and bottom can occur in form of convection cells as has been observed experimentally in the case of inhomogeneities in the amplitude of the vibration [18]. More striking is that sand spontaneously can form heaps [9 – 11] as first described already in 1831 by Faraday. Also within these heaps convection occurs which might even be the motor for the heap formation: Inside the heap the sand rises, pops out at the top and then slides down on the surface. Usually these heaps have complicated shapes that change in time and sometimes one also observes ripples and other regular structures on their surface [19]. When particles of different sizes but equal density are put on the vibrating plate the larger particles tend to rise and after some time one observes a segregation into regions with larger particles and regions with smaller particles. When the vibration of the plate also has a horizontal component the material will flow in one direction, a technique often used in powder transport.

In order to formalize and quantify the complicated rheology of granular media various attempts have been made. Continuum equations of motion and a kinetic theory [3, 20], thermodynamic formulations [21 – 23], cellular automata [24 – 26] and a random walk approach [27] have been proposed. But many of the above mentioned effects have so far eluded a satisfactory explanation of phenomena, like size segregation or density fluctuations. This is because it is very difficult to incorporate into these theories static friction, local rotations and other relevant microscopic mechanisms.

To gain a better understanding of the rheological effects of granular media it is therefore very useful to do computer simulations [28, 29]. For over a decade discrete methods have been used where instead of a continuum one treats the granular material as an assemblage of particles interacting through their contacts. This technique was introduced by Cundall [30] to study the motion of rock masses. Since then it has been applied to statistical micromechanics [31, 32], constitutive behavior of granular soils [33], creep of soils [34], analysis of rock-support interaction [35] and other applications of soil mechanics [36]. These techniques have also been applied to model size segregation [8, 37], outflow from a hopper [38, 39], shear flow [40] and flow down an inclined chute [41].

In the following we will discuss these techniques. In particular we will present Molecular Dynamics (MD) [42, 43] simulations of inelastic particles with an additional shear friction. We present data in two dimensional systems for the onset of fluidization [44, 45] and give evidence for the occurrence of convection cells due to inhomogeneities in the vibration amplitude or due to walls [46, 47]. We also report on measurements of the velocity and density profiles of powder transported on a vibrating belt [48].

A series of experiments [12, 49 – 51] have given evidence for strong density fluctuations when granular material flows under the action of gravity. Baxter et

al [12] used X-rays to visualize these wave-like patterns emanating from the outlet of a two dimensional wedge-shaped hopper. Similarly rather erratic shock-like density waves have been observed in flow through pipes [52]. Another experimentally observed ubiquitous phenomenon in granular media seems to be $1/f^{\alpha}$ noise. Baxter [53] observed power law decay in the frequency dependent forces that act on the wall of a hopper. For avalanches going down the slope of a sand pile theoretical considerations of self-organized criticality [54] led to the proposal that their size and life time distributions were power laws which was in fact only verified experimentally on very small piles [55].

In this course I will show using four models of different degree of theoretical abstraction [25, 52, 56 – 58] that the observed density patterns are composed of at least three different elements: (1) solitary waves of high density, similar to the kinematic waves of classical traffic jams, due to the concave density dependence of the flux, (2) low density waves due to the sharp increase of viscosity as function of density and (3) a background with a power-law spectrum due to self-organized criticality in the avalanches occurring inside the material because of instabilities intrinsic to inelastically colliding particles. All three phenomena are eventually consequence of dissipation and compressibility. Interestingly the fluctuations in stresses against the walls which also have a power-law spectrum don't seem to be directly related to these density patterns [59].

Loose granular media can in fact be described by a thermodynamic formalism [21] in which sand grains are treated in a similar way as molecules in a gas. This analogy reminds us that Molecular Dynamics was in fact originally developed to describe the motion of molecules.

Granular media at large densities have their own universe of funny effects. We all know that a packing of sand behaves like a solid when pushed but offers no resistance to pulling. Then there is the famous Reynold's experiment in which due to dilatancy a deformed elastic bag full of sand increases in volume when deformed. Another beach experiment [60] consists in making a sand tower having randomly spread inside some meters of fishing line. The tower withstands a considerable amount of pressure. Studying more in detail sound propagation in a granular packing shows a strong dependence of the wave velocity on pressure [61] and a subtle dependence of the local acceleration of a particle on the amplitude and the temperature due to the complex network that transmits the stresses. Large deformations of granular media occur on shear planes [62] due to a plastic instability [63].

In this course I will show results [64] of large scale MD (64.000 particles) simulations made on the CM-2 for the "mirage effect" of sound velocity and for standing waves in a rectangular box. In order to understand the formation of the fractal network of shear bands in a slowly deformed box I present results [65] from FLAC an explicit Lagrangian technique that makes use of the classical non-associate Mohr-Coulomb plastic yield criterium that is traditionally used as continuum theory for dense granular materials.

2. Molecular Dynamics Technique

As opposed to usual molecular gases the elementary units of granular materials are mesoscopic grains consisting of many atoms each ($10^{15} - 10^{25}$). When these objects interact (collide) the attractive potentials of the individual atoms are unimportant and completely different mechanisms must be considered. It is important that on a microscopic scale the surface of the grains is rough. Solid friction is the immediate consequence: When two touching grains are at rest with respect to each other a finite force F_s is needed to trigger relative motion (*static friction*), while moving against each other a finite force F_d is needed to maintain the motion (*dynamic friction*). $F_d < F_s$ and both only depend on the normal force and neither on the velocity nor on the area of contact (*Coulomb law*). No doubt, this picture is idealized and an entire discipline, called tribology, has evolved to study solid friction in depth [66]. For our purpose it is, however, more convenient to concentrate only on the basic mechanisms because we are interested in explaining the generic effects of granular rheology without entering into material-dependent details. Friction has a crucial consequence on the level of the grains, namely that the system does *not* conserve energy as opposed to what happens on the molecular level. Another source of dissipation can be plastic deformation of grains due to the normal force acting at collisions. Again it seems most important that dissipation does occur due to the normal momentum and the complications arising from the non-linearities of plasticity seems less relevant. We will therefore in the following assume very simple dissipation laws. In fact more complicated laws have been used increasing the number of parameters without giving qualitatively different answers.

Let us consider a system of N spherical particles of equal density and with diameters d chosen randomly from a homogeneous distribution of width w around d_0. When two particles i and j overlap (i.e. when their distance is smaller than the sum of their radia) three forces act on particle i:

1) an elastic restoration force

$$\boldsymbol{f}_{el}^{(i)} = k_n m_i \left[\mid \boldsymbol{r}_{ij} \mid -\frac{1}{2}(d_i + d_j) \right]^{\beta} \frac{\boldsymbol{r}_{ij}}{\mid \boldsymbol{r}_{ij} \mid} \quad , \tag{2.1a}$$

where k_n is the elastic modulus (normalized by the mass), $m_i \propto d_i^2$ the mass of particle i and $\boldsymbol{r}_{ij}$ points from particle i to j. For Hooke's law $\beta = 1$ but in the case of spheres in three dimensions one has to choose $\beta = 3/2$ [67] and for conical contacts one should take $\beta = 2$.

2) a dissipation due to the inelasticity of the collision

$$\boldsymbol{f}_{diss}^{(i)} = -\gamma_n m_i (\boldsymbol{v}_{ij} \cdot \boldsymbol{r}_{ij}) \frac{\boldsymbol{r}_{ij}}{\mid \boldsymbol{r}_{ij} \mid^2} = -\gamma m_i v_{ij}^n \quad , \tag{2.1b}$$

where γ_n is a phenomenological dissipation coefficient and $\boldsymbol{v}_{ij} = \boldsymbol{v}_i - \boldsymbol{v}_j$ the relative velocity;

3) a shear friction force which in its simplest from can be chosen as

$$\boldsymbol{f}^{(i)}_{shear} = -\gamma_s m_i (\boldsymbol{v}_{ij} \cdot \boldsymbol{t}_{ij}) \frac{\boldsymbol{t}_{ij}}{\mid \boldsymbol{r}_{ij} \mid^2} = -\gamma_s m_i v^t_{ij} \quad , \tag{2.2a}$$

where γ_s is the shear friction coefficient and $\boldsymbol{t}_{ij}$ is the vector $\boldsymbol{r}_{ij}$ rotated by 90°. Eq. (2.2a) is a rather simplistic description of shear friction. In many applications (arching, heap formation) it is important to include real static friction [68] which can be done by a static friction force [31]: When two particles start to touch each other, one puts a "virtual" spring between the contact points of the two particles. If δs is the *total* shear displacement of this spring during the contact the restoring frictional force is $k_s \delta s$ (static friction). The maximum value of the restoring force is then according to Coulomb's criterion proportional to the normal force F_n and the proportionality constant is the friction coefficient μ. Cast into a formula this gives a friction force

$$\boldsymbol{f}^{(i)}_{friction} = -\text{sign}(\delta s) \min(k_s \delta s, \mu F_n) \quad . \tag{2.2b}$$

where δs is the shear displacement integrated over the entire collision time. When particles are no longer in contact with each other the spring is removed. Main source of static friction is the geometrical roughness of the surfaces [69] and the same effects of particle stopping can be obtained also without (2.2b) by using particles of complicated shapes, like crosses or polygons [70, 71].

It is not straightforward to implement the above technique when the particles are allowed to rotate, i.e. able to roll on each other. In fact, when particles have strong deviations from the spherical shape rotations are suppressed. Often it is however useful to go an intermediate way and to include dynamic friction but not static friction and allow for the particles to have rotations [8, 38, 40]. In that case one uses a combination of Eqs. (2.2a) and (2.2b):

$$\boldsymbol{f}^{(i)}_{dyn} = -\min(\gamma_s v^t_{ij}, \mu F_n) \tag{2.2c}$$

and also introduces equations of motion for the angular momentum of the particles.

When a particle collides with a wall the same forces act as if it would have encountered another particle of diameter d_0 at the collision point. One force that acts on all particles pulling them down is gravity, $g \approx -10\text{m/s}^2$. In most simulations presented here we use a fifth order predictor-corrector MD with $10^3 - 10^5$ iteration steps per cycle depending on the largest velocities appearing in the application. This algorithm vectorizes on the Cray-YMP, running at about 10 μsec per particle-update for $N = 200$. The programs were also run on 8 or 16 processors of an Intel iPSC/860 or on an IBM RS/6000.

3. Angle of Repose and Angle of Marginal Stability

As opposed to fluids the surface of granular media at rest is usually not flat but can show undulations (ripples, dunes) or form mountains (sand piles, heaps). This is due to the fact that up to a maximal angle, the so called angle of maximal stability θ_m, grains can arrange in a statically stable way. The angle of a heap of granular material can fluctuate between θ_m and a dynamic angle θ_r. Various experiments can be deviced to obtain these angles.

Numerical studies have been made to investigate the angles θ_r and θ_m in two dimensions [68]. They start by putting N particles randomly in a box and wait sufficiently long until under the action of gravity they have all settled on top of each other and come to rest. Next one side wall is removed. The particles violently fall out forming a big avalanche and after some time only a few remain inside the box. In Fig. 1 we see the pile that is left. It forms a certain angle which is what is called the angle of repose θ_r.

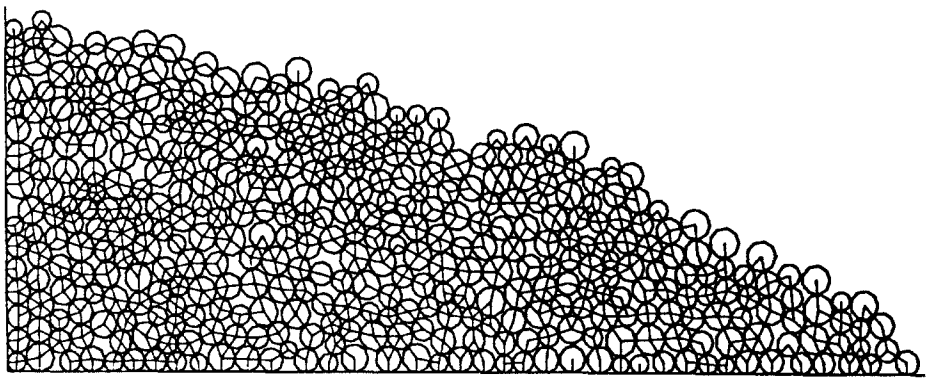

Fig. 1. Static pile obtained after the right wall from the box was removed. The parameters used are $\mu = 0.2$, $k_n = 10^6 g/sec^2$, $k_s = 10^4 g/sec^2$, $\gamma_n = 500$ and $\gamma_s = 5$ (from Ref. [68]).

In order to measure the angle θ_r from Fig. 1 one can divide the box into several vertical cells and for each cell find the highest position of the particles inside this cell. The line joining these positions can be considered as the surface of the pile. Next there are different ways to measure the slope: Either by joining the two end points, or by fitting a straight line through the points of the surface by linear regression, or by fitting a parabola through the cummulated values of the surface, etc. All definitions are slightly different but should give the same result for large enough systems.

In principle the static friction coefficient μ defined in (2.2c) should determine the slope of the pile. Since the angle of repose can easily be determined experimentally it is of interest to find the relation between θ_r and μ. In Fig. 2 we see that this relation is essentially linear for $\mu < 0.2$. Recently [72] in fact these calculations have been extended to larger values of μ and a curvature was observed which is close but not identical to the theoretical relation $\mu = tan\theta_r$. For the range of parameters which interest in practice, however, the linear relation is a very good fit.

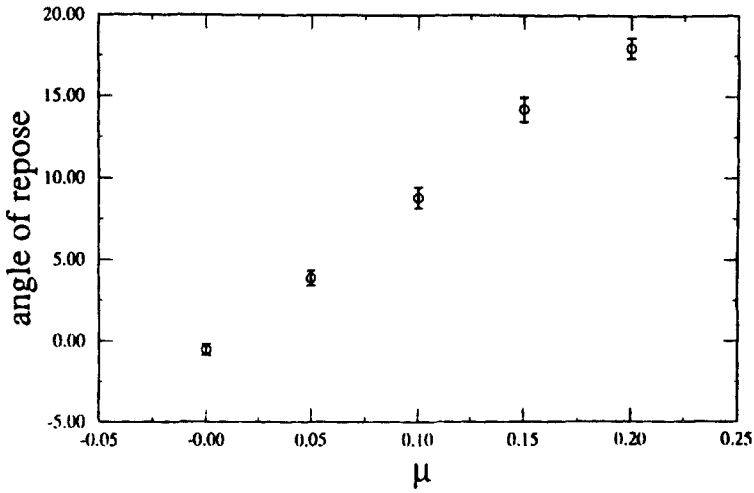

Fig. 2. Angle of repose θ_r as a function of μ for the same parameters as in Fig. 1 (from Ref. [68].

A method to obtain also the angle of maximal stability θ_m is the following [68]: Consider an empty box without a right wall and glue one layer of particles on the bottom. One monitors the largest velocity of the particles and each time this value falls below a sufficiently small value v_{max}, one inserts a new particle at the upper left corner of the box. This corresponds to experiments that have been used to measure avalanche statistics of small sand piles [55]. In Fig. 3 we show the angle as a function of time for very small piles. As predicted by the experiments [55] for such small piles the fluctuations of the angle are very large.

4. Simulating Granular Media on a Vibrating Plate

Let us now consider that the particles are placed into a container of length L that is open on the top and has either periodic boundary conditions or fixed walls in the horizontal direction. The bottom of the container is subjected to a vibrating motion described by:

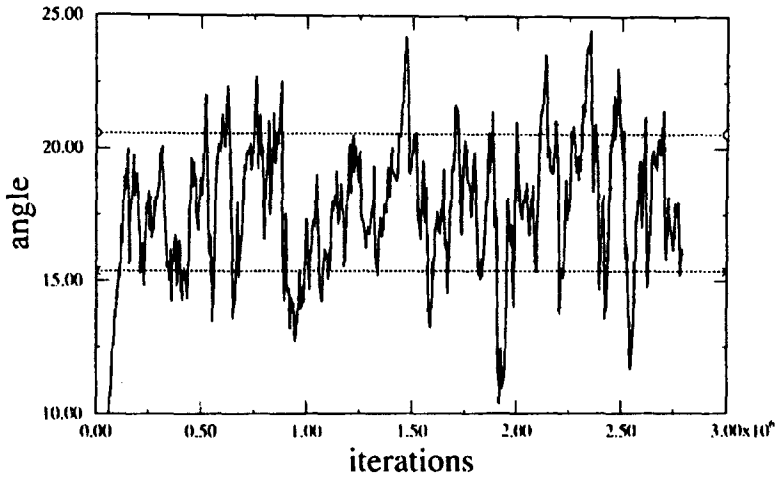

Fig. 3. Angle of the pile made by adding particles one by one as function of time (measured in MD-iterations). The dotted lines indicate the characteristic width of the fluctuations. The width of box is only four particle diameters, $v_{max} = 0.1$ and all the other parameters are the same as in Fig. 1 (from Ref. [68]).

$$z_0(t) = A(x)\sin(2\pi f t) \quad , \tag{3.1a}$$

f being the frequency and amplitude A. In some cases we will also consider an explicit spatial modulation of A of the form

$$A(x) = A_0(1 - B\cos(2\pi x/L)) \quad . \tag{3.1b}$$

For vibrating conveyor belts this plate undergoes harmonic oscillations in both horizontal (x) and vertical (z) directions according to

$$x(t) = A_x \sin(2\pi f t) \quad \text{and} \quad z(t) = A_z \sin(2\pi f t) \tag{3.2}$$

where f is the frequency and A_x and A_z are the amplitudes in x and z directions, respectively. The corresponding angle of the composed oscillation is $\alpha = \arctan(A_z/A_x)$.

Various initial positions of the particles can be considered: They can for instance be placed regularly on the bottom of the container or put at random positions inside a space several times as high as the dense packing. The initial velocities are either zero or randomly chosen. After that the particles are allowed to fall freely under gravity and relax for a time that corresponds to ten or twenty cycles of the vibration. The displacements, velocities and energies are then measured by averaging over up to 200 cycles.

Clément et al. [16] reported experimental observations of a "fluidized" state in a 2D vertical packing of steel spheres submitted to vertical vibrations. They

periodically shake (at $f = 20Hz$) 300 steel beads inside a trapezoidal cell with side walls tilted by 30^o with respect to the vertical axis. Positions and velocities of the particles were obtained by photographing the system periodically and then averaging over 15 snapshots taken at a given constant phase φ. Velocities were obtained from averages over a time interval τ around the phase φ. From a plot of the density of particles they argued fluidization to occur in the upper region of the packing. They found that the mean density does not depend on the phase of the vibration, implying the appearance of a steady state preserving the density profile at all times, independent of the up and down collective motion.

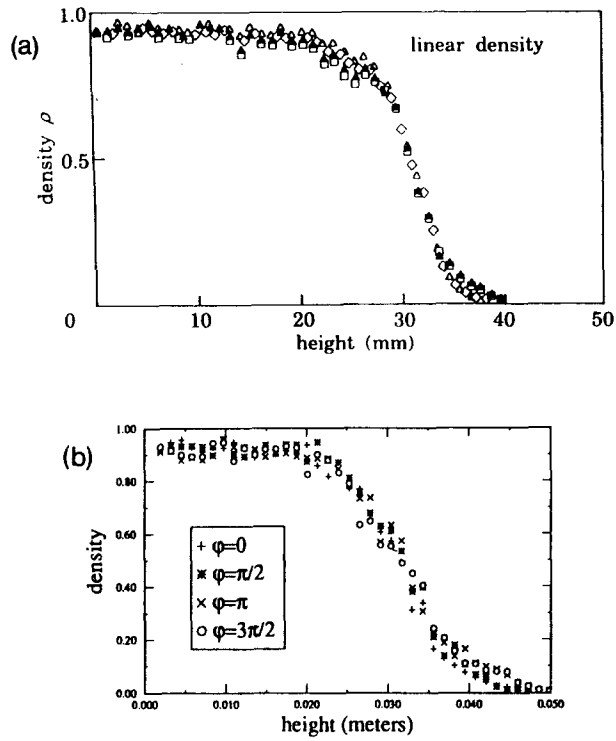

Fig. 4. Local density, normalized by the solid density, as a function of the height z for different phases of the vibration for $A = 2.5, f = 20$ Hz averaging over 30 shaking cycles after having discarded 30 cycles in order to reach steady state; (a) experiment of Ref. [16] and (b) simulation of Ref. [44].

Simulations of precisely the same geometry and number of particles as in the experiment have been performed [44] using the MD technique described in section 2 with the simplest type of friction, namely that of (2.2a). Fig. 4 shows local densities along the z-axis, evaluated at different phases as described in the

experimental paper: (a) is the experiment [16] and (b) the simulation [44]. The numerical curves were obtained by averaging the local density over the 15 ms following each phase φ and over 30 shaking cycles after discarding 30 "transient" cycles. As can be seen from this figure, the model correctly reproduces the experimental behavior of the beads, producing the same ϕ-independent, smoothly varying density profile as function of the height z. To check whether the present model is at all able to display a transition from a solid- to a fluid-like state both frequency f and amplitude A of the oscillations were varied. The trajectory of a selected "tracer" particle was monitored [44]. In the solid-like case the tracer particle remains confined to a very small region while in the fluid-like case the trajectory seems to explore the entire box. It is important to note that both situations can occur for the same value of Af^2 which means that even close to the onset of fluidization Af^2 is not a good scaling variable. It has in fact been shown [45] that in the fully fluidized regime the data can be scaled with the energy ($(Af)^2$ in one and $(Af)^{3/2}$ in two dimensions).

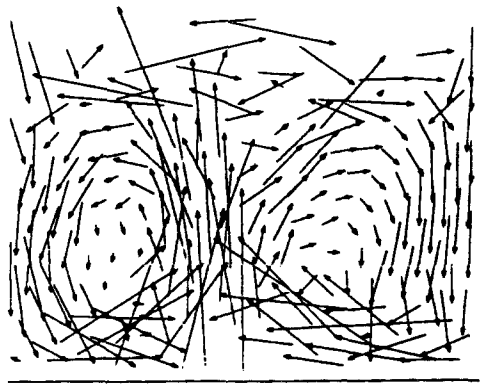

Fig. 5. Displacement of the particles after 15 cycles for $f = 70\text{Hz}$ using 200 particles in a box with periodic boundary conditions of size $L/d_0 = 20$ with $A_0 = 1.5d_0$, $B = 0.5$, $w = 0$, $k_n = 5000/d_0$, $\gamma_n = 20g$, $\gamma_s = 200g/f$, $d_0 = 1mm$ (from Ref. [47]).

Let us next consider the case of a spatial modulation in the amplitude of the vibration, i.e. $B \neq 0$ in (3.1b), using periodic boundary conditions [47] and again a friction given by (2.2a). In Fig. 5 we see the displacements of the particles after 15 cycles for $B = 0.5$. Clearly the particles flow upwards in the center where the amplitude of the vibration is larger and form two convection cells. If the dissipation coefficient γ_n is increased by a factor of ten the convection is completely suppressed while it is quite insensitive to γ_s, even if $\gamma_s = 0$. The elastic modulus also has only a very weak influence as long as it remains larger than $10^3 g/sec^2$. The initial condition plays no noticeable effect showing that convection is no transient effect. The polydispersity w of the particles only slightly distorts the shape of the convection cells.

The strength of the convection was measured quantitatively by recording the average vertical components of the velocities of the particles in the center and at the edges. These quantities have also been measured experimentally by Rátkai [18]. The strongest convection for the aforementioned parameters is obtained around 60 Hz and it increases dramatically with the amplitude A_0 as was also seen in the experiment [18]. This resonance seems to be the driving force of the convective motion.

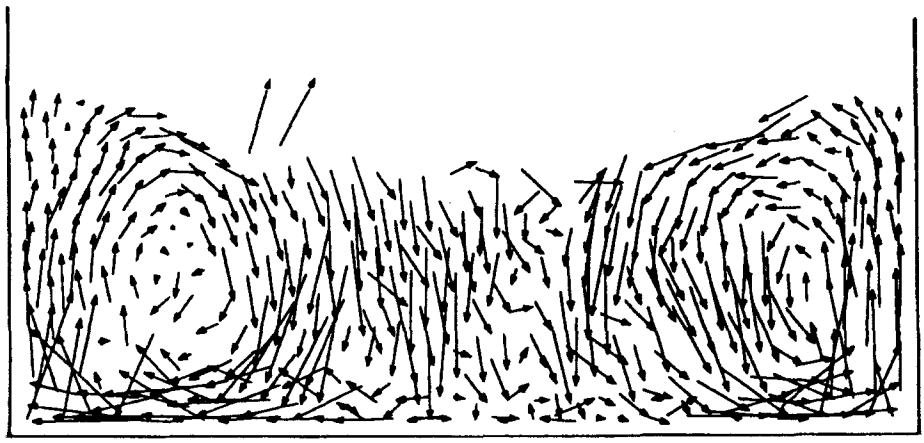

Fig. 6. Displacements after 10 cycles in a system with fixed vertical walls for $B = 0$, $w = 0.5$, $k_n = 5000g/sec^2$, $f = 20\text{Hz}$, $N = 400$, $L = 40d_0$, $A_0 = 3.0d_0$, $d_0 = 1mm$, $\gamma_n = 80g$, $\gamma_s = 0$ averaged over 10 cycles.

A completely different type of convection can be caused by the existence of fixed vertical walls without any modulation of the amplitude [47], i.e. for $B = 0$. One sees in Fig. 6 for $\gamma_s = 0$ convection cells where the motion of the particles at the wall is upward. On the other hand, when $\gamma_s \neq 0$ there is a very strong downward drag at each wall giving rise to a convection in the opposite sense. The two convection cells remain attached to the walls showing that the walls are at the origin of these cells. One also recognizes a slight heap formation close to the wall which might be a first sign of the sand heaps discovered by Faraday [9 – 11].

Let us analyze the origin of the convection due to fixed vertical walls. In the case of no shear friction the vertical walls do not transfer any vibrating motion of the container but represent only a steric hindrance to the flow. In this case, the following scenario applies: When, after levitating from the plate, the packing falls back on the bottom of the container only the horizontal component of the velocities of the particles arriving first will survive collisions with the downwards vertical motion of the rest of the packing that follows behind. So flow parallel to the bottom plate will spontaneously appear and is reinforced at each cycle. This parallel flow will only survive in regions where it is coherent and the size

of these regions will grow due to the reinforcement. When one of these regions collides with a vertical wall the flow must go upwards since it cannot go anywhere else. This explains not only the orientation of the convection but also why the convection cells are attached to the walls as seen in Fig. 6. The driving force for these cells are therefore the horizontal flows along the bottom plate.

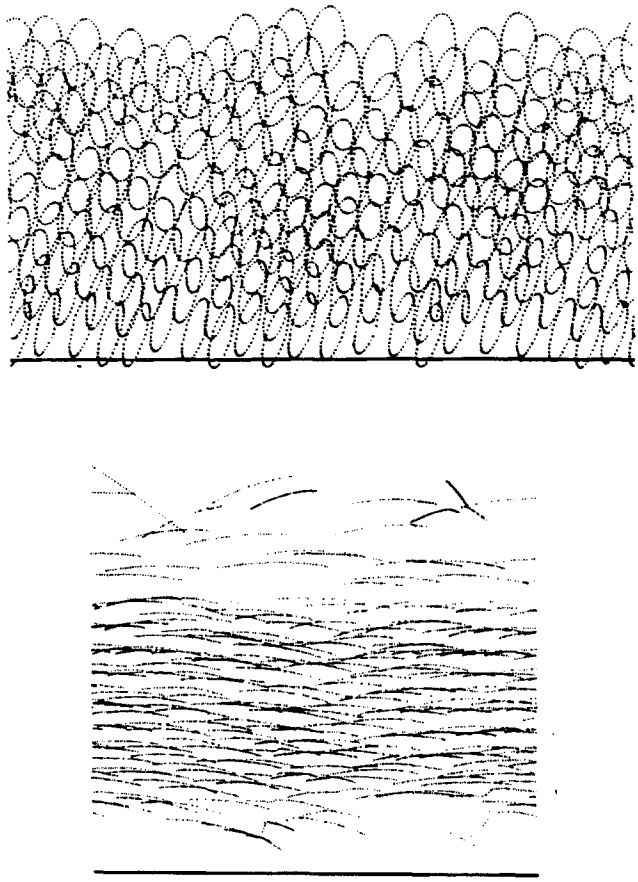

Fig. 7. Trajectories of the particles in steady state during one single cycle. The position of each particle is plotted after every 50 time-steps. The plots were obtained for $A_z = d_0$, $\alpha = \pi/4$, $\gamma_n = \gamma_s = 50g$ and (a) $f = 10$ Hz and (b) $f = 80$ Hz, top and bottom respectively.

When shear friction with the wall is present a different mechanism sets in: While the particles are pushed up and start to levitate, the packing is still quite compressed and a strong pressure is exerted on the walls giving rise to strong

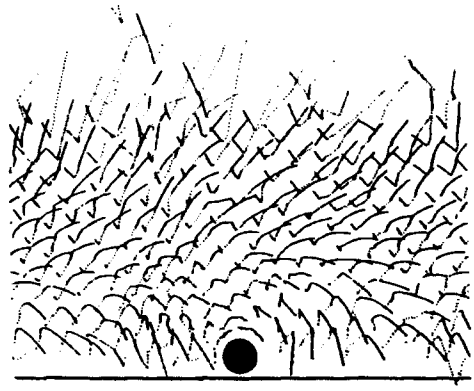

Fig. 8. Trajectories of the particles flowing in the presence of an obstacle for $A_z = d_0$, $\alpha = \pi/4$, $\gamma_n = \gamma_s = 50g$. The frequency was 80 Hz. The obstacle of diameter $d_1/d_0 = 1.5$ is given by the full circle.

shear friction while the relative motion of the particles with respect to the walls is upward. When afterwards the particles fall back and have downward relative motion with respect to the wall the packing is much looser and the shear friction much less efficient. Therefore the upward motion of the particles with respect to the wall is slowed down stronger, resulting in a net down drag along the wall. If γ_s is strong enough this effect can overcome the effect described in the above paragraph and the convection can reverse its orientation.

Let us next discuss the behavior of vibrating conveyor belts [48], i.e. granular material under harmonic vibrations having a given angle with respect to the direction of gravity as described in (3.2). Vibrating conveyor belts as a means of transportation are very typical for granular media, since neither solids nor fluids can be moved on them and are used for instance in the pharmaceutical industry to transport pills [73]. Let us consider the trajectories of the particles during one cycle of shaking. When the frequency is low enough all the beads move synchronously along elliptic trajectories curves as shown in Fig. 7a. The tilting angle of these ellipses increases with the angle of vibrations. For smaller shear friction coefficients γ_s the tilting angle tends to $\pi/2$, provided the vibration frequency is low enough. When the beads start to flow, the character of their trajectories changes: at not too high frequencies they move along sinusoidal. With increasing frequency, the trajectories become flatter and at the highest frequencies we observe a nearly horizontal flow (see Fig. 7b). A decrease of the vibration angle makes the horizontal motion more pronounced. A similar effect occurs when the friction coefficients are increased. For vanishing shear friction γ_s the beads move essentially vertically.

It is also interesting to check how a circular obstacle inserted into the system influences the flow. To this end, a fixed circular body can be inserted at $x_1 = L/2$, $z_1 = A_z$. The diameter of this obstacle has been varied from $d_1 = 0.1d_0$ to $d_1 = 2.5d_0$. The parameters characterizing the interactions of the obstacle with the particles are the same as in the case of particle-particle interactions. Note that due to the periodic boundary conditions, the obstacle is repeated along the belt. Even the presence of a rather small obstacle rapidly slows down the flow. In Fig. 8 we see the trajectories of the particles for an obstacle of $d_1 = 1.5d_0$. Figs. 7b and 8 have the same parameters so that without the obstacle Fig. 8 would look like Fig. 7b. Clearly the presence of the obstacle changes the trajectories of all the particles considerably. So, we cannot treat the obstacle as only locally influencing the flow, because the stiff repulsion between particles generates long-range correlations.

5. Simulating Size Segregation

One of the most puzzling phenomena encountered in granular matter is size segregation: When a mixture of grains of the same material (equal density) but different size is shaken in a container the larger particles rise to the top. This effect has been extensively studied experimentally [5, 74, 75] and has much importance in numerous industrial processes [76]. Recently this so called "Brazil nut effect" has attracted much interest among physicists [2].

Size segregation inevitably seems to contradict equilibrium statistical mechanics since the density of the overall packing increases with polydispersivity and so gravity makes situations with larger particles on the bottom energetically more favorable. Rosato et al. [6] proposed a Monte Carlo algorithm and put forward a kinetic argument to explain segregation using the fact that smaller particles are more mobile. In the same year Haff and Werner [8] did Molecular Dynamics simulations of rather small systems and claimed that segregation was essentially a consequence of solid friction and the rotation of the particles. Jullien et al. [7] used a piling technique which is non–stochastic as compared to the one of Ref. [6] and found a critical ratio $\mathcal{R}$ for the radia of spherical particles below which no segregation occurs. Based on these ideas Duran et al. [77] formulated a geometrical theory for segregation in which the small particles glide down along the surface of the larger particle, the critical ratio $\mathcal{R}$ of radia being between continuous and discontinuous gliding. They also claimed experimental evidence for two types of dynamics and visualized the discontinuous ascent of the larger particle through stroboscopic photos. Jullien et al. [78] reproduced the discontinuous dynamics by including horizontal random fluctuations into their model.

Parallel to these local theories there has been the "convection connection": It is known experimentally [18] and numerically [46, 47] that shaken assemblies of spheres form convection rolls which are attached to the walls of the container. For weak shaking the convection rolls only appear on the surface. Knight et

al. [79] showed experimentally that segregation was due to this convection and the fact that larger particles have a harder time entering again into the bulk once they are on the surface. They also verified an exponential decay of the convection strength as function of depth for weak shaking [80]. Duran et al. [81] verified segregation due to convection in two dimensions for strong shaking and claimed that above mentioned local mechanisms are at work at weak shaking. Their stroboscopic pictures showed convection cells above the particles.

Large scale Molecular Dynamics simulations show [37] that also for weak shaking convection is responsible for segregation but in a more intricate way: Under certain conditions the larger particle is able to pull down the convection rolls due to the more efficient momentum transfer and then rise within its flow. Because of the exponential decay of convection with depth the ability to rise critically depends on the vertical position of the larger particles.

Throughout the simulation the parameters were $k_n = 3 \cdot 10^6\ g/sec^2$ (elastic modulus), $\gamma_N = 100\ Hz$, $\gamma_S = 1\ Hz$ (phenomenological normal and shear friction coefficients) and $\mu = 0.5$ (Coulomb friction parameter). We considered $N = 950$ particles were considered with diameters uniformly distributed in the interval $d_i \in [1.7, 2.3]\ cm$ and with masses $m_i = 2\pi R_i^2 \rho$, $\rho = 1\ g/cm^2$. The particles are put into a two–dimensional box having walls made of particles with the same material characteristics as the grains and which vibrates vertically according to $z_0(t) = A \cdot \sin(2\pi f t)$ with $A = 2\ cm$. Gravity acts in negative z–direction $F_i^{gr} = -m_i\ g$, $g = 981\, cm/sec^2$. The time step for the numerical integration of the Gear predictor–corrector scheme of 5th order was $\Delta t = 5 \cdot 10^{-5} sec$.

Segregation and convection behavior have been investigated [37] as function of the vibration frequency f in two different systems, either all particles are small or we add one single big particle of radius $R_1 = 4\ cm$ located in the center of the box close to the bottom. In order to investigate closer what happens at the onset of segregation we keep all the other parameters fixed. Fig. 9 shows the convection cells without the larger particle (left) and with the larger particle (right) for the frequency $f = 2.8\ Hz$, i.e. at the onset of segregation. The convection cells with and without the big particle, differ significantly while they are quite similar for larger or smaller frequencies. This indicates that at the onset the presence of the big sphere triggers the onset of convection which finally leads to segregation. Indeed we find that convection is always present when segregation happens. It is important to note that if one is close enough to the onset of segregation just putting the larger particles one row lower can entirely suppress the effect of segregation. This dependence of segregation on the height is quite strong and has not been discussed in the literature. By changing the frequency f very slowly and measuring the convection flow through a plane at a certain height we observed that the transition from the fluctuation regime to the convection regime is very sharp within the numerical precision ($\Delta f = 0.05\ Hz$). Moreover, when increasing the frequency the transition occurs almost exactly at the same frequency as when decreasing the frequency, i.e. there is no hysteresis.

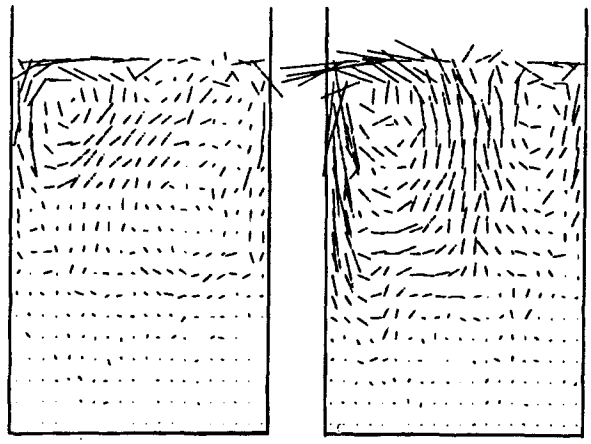

Fig. 9. Convection rolls in systems without (left) and with the larger particle (right) for $f = 2.8\ Hz$. The big particle triggers convection rolls. The velocities were obtained by averaging over 50 shaking periods of the box (from Ref. [37]).

The triggering of convection cells by the big particle is investigated more quantitatively by calculating the convective flux Φ defined as the sum of material (mass) flow in the center of the box j_{top} and the flow close to the walls j_{bot} by considering that these flows have opposite signs. The flows j_{top} and j_{bot} are defined by adding the number of particles which move in one direction minus the ones moving in the opposite direction and is measured in particles per cycle time. In fact we measure for each particle if the positions at subsequent nodes of the vibration are on different sides of a height line, where the height of the box was divided into 80 height lines between the bottom of the box and the surface of the packing. Fig. 10 shows the convective flux Φ through planes at different heights D for both systems and for the three different frequencies. For $f = 2.6\ Hz$ we find almost no directed flow but only fluctuations. For $f = 3\ Hz$ both systems, with and without large particle, behave similarly, as could also be observed in Fig. 9. For $f = 2.8\ Hz$, however, the convection cells clearly extend deeper due to the existence of the larger particle. Apparently the larger particle is able to pull the convection cells down.

This effect can be explained by the fact that in the region around the large particle the accelerations are higher since the momentum is transferred with less dissipative loss through the larger particle than through a corresponding pile of smaller particles of the same volume. We measured the sum of the absolute values of the forces of all the particles in a region around the position of the large particle and averaged it over time. The region was ring shaped with the inner border of radius 4.5 *cm* and the outer border of radius 8 *cm*. At the onset

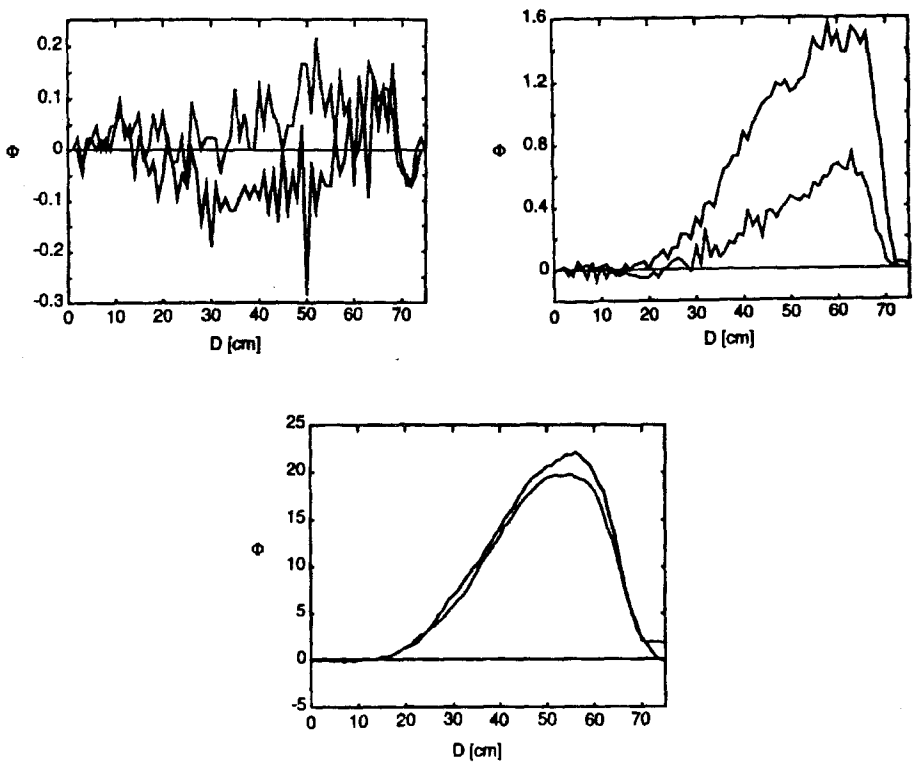

Fig. 10. Strength of the convection rolls measured through the flux Φ as a function of the height D, $f = 2.6\ Hz$ (upper left figure), $f = 2.8\ Hz$ (upper right figure) and $f = 3\ Hz$ (lower figure). The height D is measured such that the bottom is at the origin of the axis. The flux Φ is measured in units of particles per period. In the central case the convection rolls are stronger and reach deeper inside the material in the presence of the big particle. This triggered convection roll catches the big particle and forces it to rise to the top. (from Ref. [37])

of segregation ($f = 2.8\ Hz$) the average force of the small particles around the large particle is about 15% larger than that of the small particles in the same region in a system containing no large particle. This effect is strongest in the lower part of the ring shaped region. For $f = 2.6\ Hz$ the difference is only 5%. Therefore the accelerations in the region around a large particle are larger than if no particle would be present. We believe that this increase in high frequency oscillations is responsible for pulling the convection rolls down. It is, however, interesting to note that the granular temperatures (kinetic energy) in this region is roughly the same in the two systems.

One can see from Fig. 9 that the convection cells decay very sharply in strength but that even in the deep regions some essentially horizontal motion occurs. This is reminiscent of the stroboscopic pictures of [81] implying that even in the low acceleration regime some particles move inward horizontally. Within

our framework this motion could be interpreted as the exponentially weak tail of the convection rolls.

Next we investigated the dependence of the onset of convection on the ratio of radia $\mathcal{R}$. Note that in our case $\mathcal{R} = R_1/1cm$ because the mean radius of the small particles is $1cm$. For $f = 3.2\ Hz$ we observed a big particle of radius $\mathcal{R} = 4.0$ moving up immediately. We also studied the cases $\mathcal{R} = 3.5$, $\mathcal{R} = 3.0$, $\mathcal{R} = 2.5$ and $\mathcal{R} = 2.0$. In these cases the large particle remains a certain waiting time on the bottom before it suddenly moves up quite rapidly. Fig. 11 shows a typical evolution of the vertical position of the big particle with $\mathcal{R} = 2$. The waiting times do not noticeably depend on $\mathcal{R}$ being of the order of 30 *sec*. Once the large particle comes to the top it performs an oscillating motion going up and down (whale effect) that has also been observed experimentally [82]. This motion seems due to the convection rolls: In the case where $\mathcal{R}$ is smaller the oscillating motion is more regular because the larger particle has less difficulty reentering into the bulk from the surface and follow the convective motion. For larger $\mathcal{R}$ the larger particle has more difficulty reentering thus leading to a more erratic horizontal motion. Particles with smaller $\mathcal{R}$ also seem to dip deeper into the bulk showing that the convection cells can move them more efficiently.

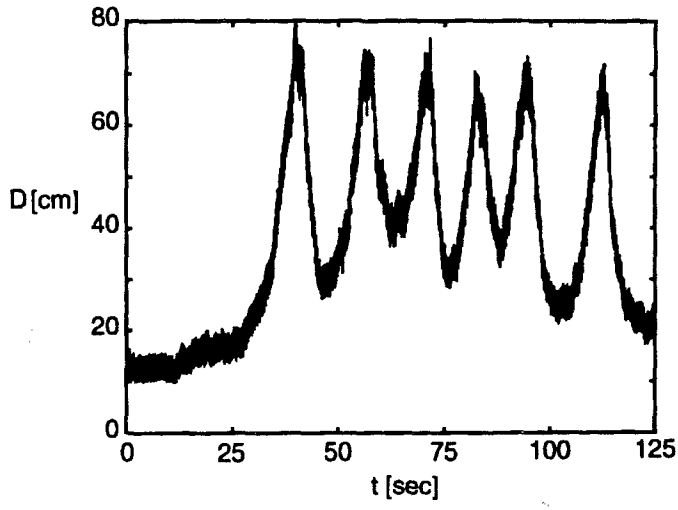

Fig. 11. Evolution of the vertical position of the big particle as function of time, $\mathcal{R} = 2.0$ for $f = 3.2\ Hz$ (from Ref. [37]).

Concluding, it seems that segregation of granular media in a vibrating box in two dimensions is intimately connected to convection. The larger particles, surrounded by a region of higher acceleration, loosen the material thus deepening the penetration of the convection rolls from the top into the medium. After some waiting time the larger particles are caught by the lower part of the rolls and pulled up. This triggering effect is only relevant close to the characteristic onset

frequency of segregation which is sharply defined and strongly dependent on the initial depth of the large particle. Once the large particle is on the top it periodically goes up and down (whale effect) driven by the convection cells.

In addition to convection arching and geometry are also important as pointed out by many authors. How the large particles move in the exponentially weak convection field before being lifted upwards and the $\mathcal{R}$-dependence of the mobility are probably best described by Duran et al.'s local arching mechanisms [77, 81]. The fact that the whale effect of larger particles is less pronounced is certainly due to their lower mobility because of steric hindrance effects as formulated by Rosato et al. [6].

Many of the details of segregation are still not completely clear and in particular in three dimensions additional geometrical effects might play a role. This as well as other questions are difficult to study conclusively with a numerical technique due to the excessive requirements in computer time. It would for instance be interesting to see what happens when the box is so wide that the walls of the box are much farther away from the large particle than the height of the packing. In this experimentally relevant case the walls would not be able to stabilize the convection rolls. Simulations with periodic boundary conditions have, however, provided rather similar results as with fixed boundaries [83]. It would also be interesting to study larger ratios $\mathcal{R}$ in order to verify predictions made about a characteristic value of $\mathcal{R} = 12$ [7, 77] but for that case one would need to consider substantially larger systems. Three dimensional calculations have been made [83] but there the length scales are even smaller. The limitations in observation time due to the computational requirements also puts limits on the determination of the segregation velocity and we cannot exclude that particles rise on time scales much larger than the ones accessible numerically.

6. Simulating the FlowThrough Hoppers and Pipes

The outflow of granular materials from hoppers and silos is an important technological problem although it seems to be so commonplace and low-tech. After many years of uninterrupted service a silo might one day suddenly succumb under a "siloquake" or similar shock phenomena of surprising violence causing considerable harm. In fact silos and similar recipients are by orders of magnitude the industrial structures most susceptible to collapse. The reason for these catastrophic events are that the forces exerted by the flowing granular material against the wall of the container can fluctuate in magnitude by many orders.

Using similar techniques as in the last section but including the Coulomb (dynamic) friction of (2.2c) and rotations of particles as in Ref. [8] simulations were made for the flow out of a hopper [38, 56] and flow through a pipe [52].

The simulations for the flow out of a hopper [38] find the existence of a minimal outlet diameter below which clogging occurs due to arching which is larger for equal sized particles than for randomly distributed radia. In fact the rheology of the particles is very different when they are monodisperse: For a

random distribution of radia the acceleration occurs on a ramified structure that has strong temporal fluctuations. Particles of equal size form regular, crystal-like domains and the motion occurs between the blocks. This bloc motion has been described in detail in the experiments of Drake [84].

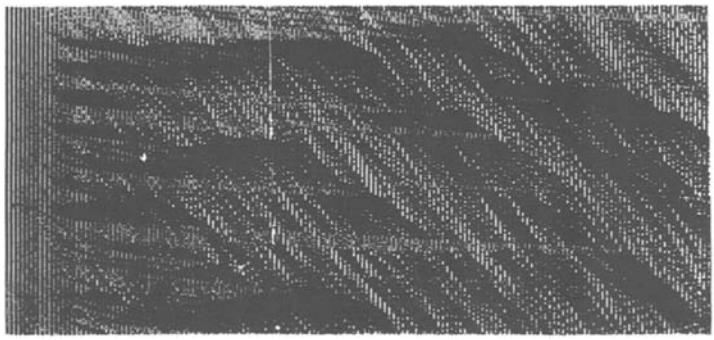

Fig. 12. Vertical pipe plotted at regular time steps next to each other. Time goes from left to right. Gravity acts from top to bottom. For more details see Ref. [52].

In Fig. 12 we see a space-time diagram of the density inside a pipe with 600 particles and periodic boundary conditions. The particles initially have randomly distributed initial positions and velocities (left pipe). After some time spontaneously various patterns appear in the density: On one hand one has very dark regions, nearly constant in time. Then one sees black diagonal stripes of constant velocity down the pipe. Finally there are also some lighter horizontal lines. In the following we want to try to explain these rather complex structures.

Similar effects have also been observed in hoppers of opening angles of $\theta = 30°$ and the density at a position six particles diameters above the outlet has been measured as a function of time [56]. In Fig. 13 we see the Fourier transformation of this density in a log-log plot. Clearly the data fall on a straight line over nearly two decades. The slope is about $\alpha = -1.35 \pm 0.1$ obtained by a least square fit. That means that we have a power law spectrum of the form $1/f^{\alpha}$.

When particles of equal size are taken we observed equally well developed density patterns and find roughly the same power law decay of the spectrum. The effect is reduced when the diameter D of the outlet becomes too large. If it is too small the flow of particles can entirely stop due to arching. The critical diameter D_0 when this arching sets in has been studied before with similar techniques [38] where it was found that D_0 is larger when the particles have the same size. When we consider smooth walls, i.e. all wall particles having the same radii, we do not find density waves and the power spectrum looks significantly

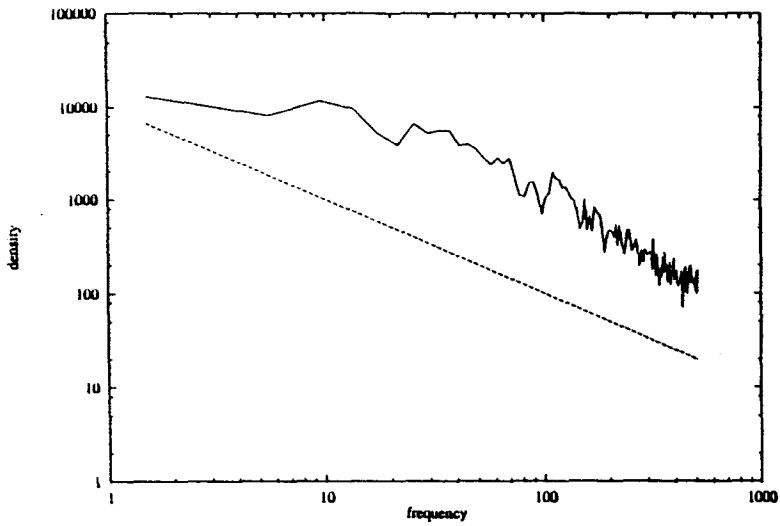

Fig. 13. Log-log plot of the spectrum of the density fluctuations in a hopper [56]. The elastic modulus is $k_n = 10^6 \mathrm{g/s}^2$ and the time step $\Delta t = 2 \cdot 10^{-4} sec$.

different. It shows an upwards curved slope with increasing frequency which one also finds when configurations block during the outflow. A similar effect was also found in simulations of flow on an inclined plane [41].

Baxter et al. [53] also measured the stresses acting on the walls of a three dimensional hopper with an opening angle of 45° during the outflow of sand. They observed a power law decay in the spectrum of the time dependence of the normal stress (pressure) where the exponent strongly depended on the run.

The stresses acting against the walls have been measured [59] by taking from our algorithm the normal p and tangential τ components of the force acting against each of the particles of the walls and monitor the time dependence of the stresses at a given position on the wall. The fluctuations of the first invariant of the stress tensor, defined as $\sqrt{p^2 + \tau^2}$, are of the same order as the values themselves. No apparent correlations are visible. In order to get a more quantitative information we show in Fig. 14 the power spectrum of these time sequences, i.e. we took the square of the amplitude of its Fourier transformation. For sufficiently open hoppers, like for $\Theta = 55°$, the spectrum decays with a power law over at least one order of magnitude with an exponent of about 1.3. This is in very good agreement with the experimental results of Baxter et al. [53] which worked at the same opening angle; (they define the angle as $90° - \Theta$). Their power law, however, extends over a much larger range than in the simulation because the computer requirements limit the observation times to several minutes while the real experiments can be carried out over many hours.

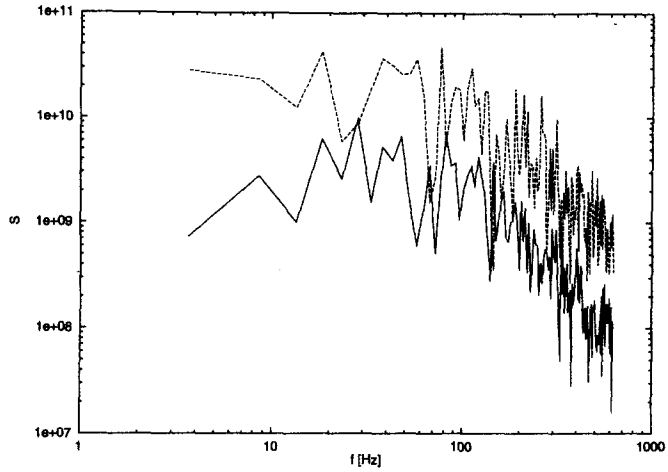

Fig. 14. Log-log plot of the power spectrum of the stresses for $\Theta = 60°$. The upper curve corresponds to the shear stress and the lower curve to the pressure. The slopes are -1.4 (top) and -1.7 (bottom). The opening had a diameter of ten particles.

It is very interesting to note that if the hopper walls become more inclined the spectrum changes abruptly and becomes white noise. Savage [85] found a similar situation in numerical calculations of the wall stresses in shear cells as function of density: Only at rather high densities the power spectrum showed a power law while for lower densities he observed white noise. In our case although the density cannot be varied a change in the opening angle determines if there are stagnation zones or not and evidently the density in the flowing regions is lower than in stagnations zones.

The observed shapes of stagnation zones in real three dimensional silos are curved, either cusplike downwards for primary flow or S-shaped for secondary flow [86]. Indeed the shape of the stagnation zone as found numerically become S-shaped after some transient time. Only close to the outlet the shape remains linear. The acceleration zones inside the flowing part have elliptic shape also in agreement with the observations of the inner core of the flow [86]. It seems that the fact that these observations were made on three dimensional hoppers while the numerical simulations are two dimensional (with exception of the Hertzian contact law) does not influence the qualitative picture very much.

It is interesting to see how the shape of the stagnation zone depends on the opening angle of the hopper Θ. For that sake also the case $\Theta = 0$, i.e. a box with a flat bottom was simulated. In this case the S-shape of the stagnation zone reaches down to the edge of the outlet in even closer agreement with the typical observations.

Investigating with large scale MD simulations the force distribution and the shape of the stagnation zones of outflowing hoppers one therefore has an interesting dependence on the opening angle: In the case of funnel flow ($\Theta = 75°$) there are no stagnation zones and the power spectrum of the stresses against the walls

has white noise. Opening the angle one finds stagnation zones and a power law spectrum. This leads one to suspect that the power law in the stress spectrum does not originate from the power law in the density fluctuations [12, 56] because the density fluctuations also follow a power spectrum in the case of funnel flow. It seems more likely that the stagnation zones act like "noise transformers" in which essentially uncorrelated random kicks coming from the outflowing core are transmitted through the complex contact network to the wall and arrive power-law correlated. Similar observations have been made with the propagation of shock and sound waves in dense packed boxes [13].

7. Traffic Models

We have shown that similar to the avalanches that one observes on the surface of a sand pile also inside the bulk of granular material one has avalanche behavior which like the ones on the surface shows self-organized criticality on small scales [54]. The mechanisms that generate the patterns are similar but not identical to the original sandpile models. While the static friction similarly generates waiting times with a threshold it is not the motion of the sand itself that constitutes the avalanches but it is the group velocity of the holes between them: An individual particle can easily go from one dense region to the other by flying fast through a region of low density. There is therefore a backflow of information similar to the jamming on highways [87].

Everybody knows of the seemingly erratic motions of cars jammed on highways. One wonders whether they are due to a random behavior of the individual drivers or if there is an intrinsic chaotic mechanism. In favor of the first hypothesis is the existence of regular kinematic waves in dissipative systems with excluded volume [88]. For this reason many traffic models include rather important statistical noise in time [87]. In favor of the second hypothesis are measurements performed on Japanese highways showing a $1/f$ spectrum in the Fourier transformed density fluctuations [89] which might stem from some self-organized criticality [54]. It is therefore interesting to see if a traffic model without noise is able to give the observed erratic behavior and its $1/f$ spectrum.

In Ref. [57] we consider a continuous one-dimensional model. The system has length L with periodic boundary conditions; and the velocity v_i and position x_i of a vehicle i are continuous variables. The update rule is defined as follows:

- If the velocity is high with respect to the gap, then the car slows down:

$$\text{if} \quad v > \Delta x - \alpha \quad \Rightarrow \quad v \to \max(0\,,\,\Delta x - 1)\,; \tag{7.1a}$$

  (the "max" is only necessary to prevent negative velocities);
- else if the velocity is low with respect to the gap and slower than five, then the car accelerates:

$$\text{if} \quad v < \Delta x - \beta \ \text{ and } \ v < v_{max} \quad \Rightarrow \quad v \to v + \min(1\,,\,\gamma * \Delta x)\,. \tag{7.1b}$$

Arbitrarily one can choose the maximum velocity to be $v_{max} = 5$ so that this rule allows maximum speeds up to nearly six.

- After the velocity has been updated for all vehicles according to the last two rules, we move all vehicles simultaneously by a distance equal to their velocities.

In Ref [57] initially $N = [\rho \cdot L]$ vehicles were placed on equally spaced sites 1 to N, all with velocity zero, where the total number of cars ρ was chosen small enough to prevent the first car hitting the last one through the periodic boundary conditions. Starting from this totally ordered initial state, the system is allowed to evolve according to the above rules, with the restriction that the first vehicle has a speed kept fixed at $v_{lead} = 4.99999$. This is a simplification of the well known situation where fast vehicles follow a slower one which they cannot pass.

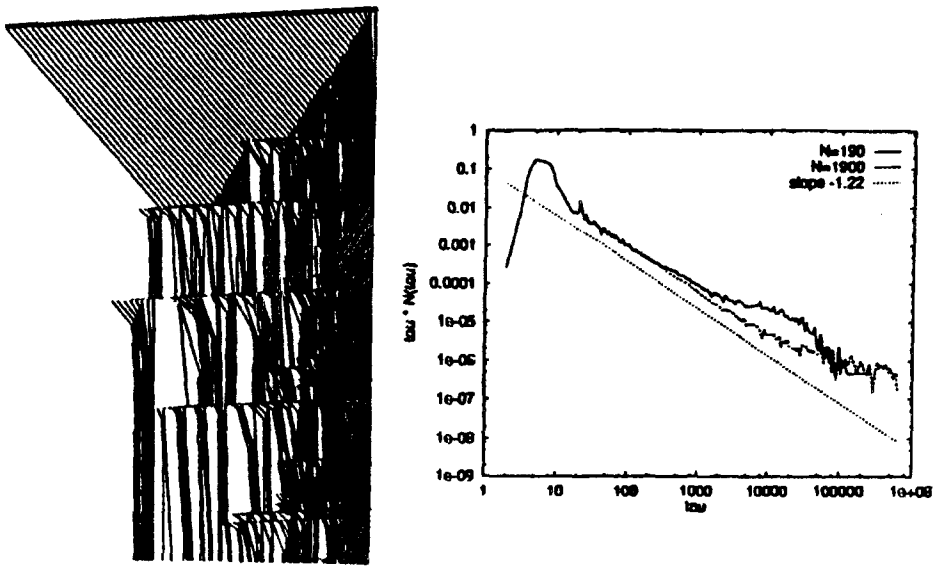

Fig. 15. Left: First 4200 time steps (from top to bottom) and flow of $N = 61$ cars from left to right on a lane of length $L = 1024$. Right: Distribution $n(\tau)$ of times τ between consecutive breaking events for $N = 190$ and $N = 1900$ cars; $\alpha = 0.5$, $\beta = 3.0$, and $\gamma = 0.1$ (from Ref. [57]).

In Fig.15(left) we see the time evolution of a system which has been transformed to the coordinates of the first vehicle, i.e. the positions of all cars are given relative to the first car. We see that equally spaced cars rapidly evolve into a fluctuating state (right hand side). In this new state density increases give rise to very short bursts (traffic jams) of very different sizes which redistribute the

cars backwards such that in some cases they even start again in equally spaced patterns.

In order to ensure that this behavior is an intrinsic consequence of the dynamics and not just the enhancement of numerical round-off errors, single precision and double precision calculations have been compared to each other. The behavior of the model (i.e. the formation of the collective shocks) is robust with respect to parameter changes. More precisely, no qualitatively different behavior for changes of the parameters α, β, γ, and v_{lead} has been observed within the following range $0.1 \leq \alpha \leq 0.6$, $2.0 \leq \beta \leq 5.0$, $0.08 \leq \gamma \leq 0.12$, $4.5 \leq v_{lead} \leq 4.99999$.

One can also measure the distribution of times τ between consecutive "braking" events for the last vehicle (τ counts the time from the end of one braking to the beginning of the next). Braking is defined as a slowing down according to the rules for the velocity update.

For $N = 1900$ vehicles, after about $3 \cdot 10^5$ time steps to let the transients die out the distribution of τ was measured during about $1.1 \cdot 10^6$ further time steps. As seen in Fig. 15b, this distribution displays a remarkable straight line on a log-log plot, fulfilling a power law relation

$$n(\tau) \propto \tau^{-\alpha} \tag{7.2}$$

with $\alpha = -2.2 \pm 0.1$. This is an indication for the existence of self-organized criticality [54].

Many aspects of this model are remiscent of the so-called train model for earthquake dynamics [90]. Instead of pulling at one end, the slower car may be seen as pushing against the other cars which want to move faster. This leads to a slowly increasing average density, and at some time this density locally exceeds a critical threshold. The reaction is a more or less drastic slowing down of the corresponding vehicle, which may or may not force the next vehicle to slow down as well. By this mechanism, avalanches of all sizes are generated, which may propagate through the entire traffic jam.

8. Lattice Gas and Boltzmann Lattice Models

It seems natural to describe the flow of granular media using the concepts of fluid mechanics. One must, however, consider that as opposed to classical fluids there is local dissipation of energy. Taking into account the dissipation rate in the energy balance equations it has been possible [91, 92] to predict the existence of an instability: Slightly denser regions have more dissipation and therefore lower pressure which itself generates a flow that will enhance the density. So, the dissipation will be responsible for the formation of clusters of high density and these have been observed [91]. Also has it been possible to derive from this kinetic gas theory [92 – 94] that the viscosity increases very sharply with density.

One alternative to the direct solution of the equations of motion of fluids are the so called Lattice Gas (LG) [95] Lattice Boltzmann Models (LBM) [96]. These

models are defined on a lattice with velocity vectors that can only point into few discrete directions and all have the same length. For the LBM this simplification is somewhat compensated by the fact that on each site one has more real degrees of freedom (six on a triangular lattice) than in the classical numerical techniques allowing for the definition of a local shear or a local rotation.

Let us first describe the Lattice Boltzmann Model as used in Ref. [58]. We consider a triangular lattice, and on each site $\boldsymbol{x}$ we have six real variables $N_i(\boldsymbol{x}, t)$, $i = 1, ..6$, representing (counted counter clockwise) the densities of the particles going in the direction i of the lattice. (For convenience we will in the following omit the site index $\boldsymbol{x}$ and denote by N_i' the value of the particle density after collision.) One updating of the system ($t \rightarrow t + 1$) is given by two steps: (1) The collision step at which the six N_i are updated at each site through

$$N_i' = N_i + \lambda(N_i - N_i^{eq}) \tag{8.1}$$

and (2) the propagation step at which each N_i is shifted to the site of the nearest neighbor in direction i. Eq.(8.1) produces a relaxation towards the equilibrium densities N_i^{eq} which is numerically stable provided $-2 < \lambda < 0$. The value of λ sets the kinematic viscosity ν of the fluid. The equilibrium densities in (8.1) are given by

$$N_i^{eq} = \frac{\rho}{6}(1 + 2\boldsymbol{u} \cdot \boldsymbol{c}_i + 4(\boldsymbol{u} \cdot \boldsymbol{c}_i)^2 - 2\boldsymbol{u}^2) \tag{8.2}$$

where ρ is the mass density at site $\boldsymbol{x}$

$$\rho = \sum_i N_i \quad , \tag{8.3}$$

$\boldsymbol{c}_i$ the unit vector along direction i and $\boldsymbol{u}$ the velocity at site $\boldsymbol{x}$ defined through the momentum density per site

$$\rho \boldsymbol{u} = \sum_i \boldsymbol{c}_i N_i \quad . \tag{8.4}$$

The equilibrium distribution N_i^{eq} given in (8.2), is chosen to give mass and momentum conservation in the collision step. The flow will be forced into the direction of gravity $\boldsymbol{g}$, which is pointing parallel to the walls of the pipe. For that purpose an additional step is added after the collision step which is defined by $N_i'' = N_i' + \frac{1}{3}\boldsymbol{c}_i \cdot (\rho \boldsymbol{g})$. Periodic boundary conditions are imposed in the direction of gravity in which the system has a length of L. In the perpendicular direction one has walls separated by W lattice spacings. The lattice orientation is such that one of the lattice directions is parallel to the walls at which no-slip conditions are used. At the beginning of the simulation the average density $\bar{\rho}$ is fixed. It is an important parameter of the model which because mass is conserved.

The relaxation parameter λ depends on the material properties including the kinematic and the bulk viscosities. Since an exact relation between λ and the material constants is not known we will lean on some approximative arguments [95] that predict a vanishing bulk viscosity. In that case one can relate λ directly to

the kinematic viscosity ν through $\lambda = -\frac{1}{2}(0.25 + 2\nu)^{-1}$. We will consider that ν is a function of the local density ρ.

A salient feature of granular media is the spontaneous formation of density waves, similar to traffic jams of the previous section. One possibility to explain the effect that generates these waves is to assume that the viscosity depends on density. Within the kinetic gas theory of granular media [92 – 94] the relation $\nu \propto (\rho - \rho_c)^{1/3}$ has been derived. Since the above relation imposes a maximum density ρ_c it is rather difficult to implement it directly within the context of the LBM where the particles do not have an excluded volume. We therefore chose a piecewise linear relation of the form $\nu = \nu_{min}$ if $\rho \leq \rho_t$ and $\nu = \nu_0 + \gamma(\rho - \bar{\rho})$ for $\rho > \rho_t$ (see Fig. 16a). $\bar{\rho}$ is the average density and the threshold density ρ_t is chosen to make ν a positive continuous function of the density. We initialize the system by having the same values of the N_i on each site and then let the system evolve to its steady state. In the case of stable flows steady state is reached after 2000 or 3000 time steps. In the case of the unstable flows that develop density waves, the simulations might take up to 20000 time steps to reach steady state.

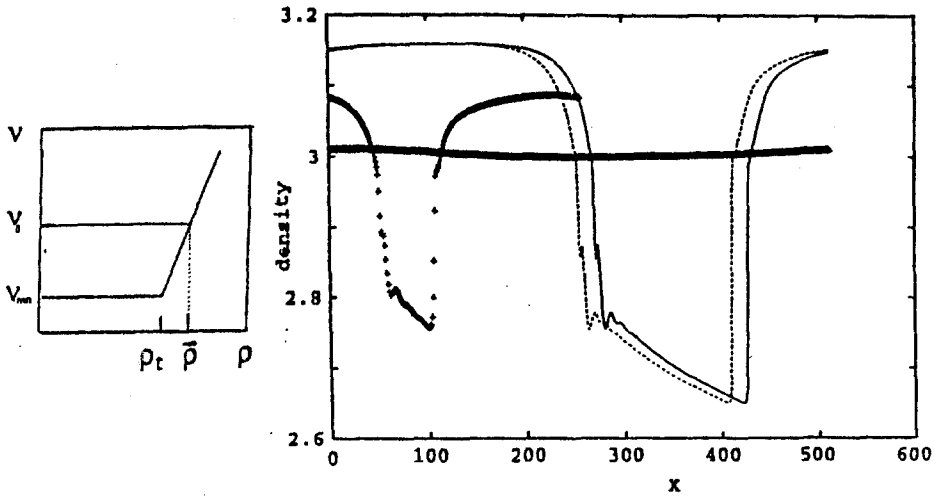

Fig. 16. Left: Density dependence of the viscosity chosen in the simulations. The slope is $\gamma = 6.25$ and the minimum viscosity is $\nu_{min} = 0.01$. Right: Density in the center of the channel as a function of the position X along the channel for $\rho_t = 2.962$, $\bar{\rho} = 3.0$, $g = 3.33 \times 10^{-5}$ and $W = 64$. The crosses are for $L = 256$ and 60,000 iteration steps after the initial perturbation. The other curves correspond to $L = 512$ for 5000 (thick line), 60,000 (full line) and 60,025 (dashed line) iterations after the perturbation was applied (from Ref. [58]).

In order to generate density waves it is necessary to introduce a small perturbation producing a 0.3% relative density difference on one line across the pipe, keeping the mass unchanged [58]. In Fig. 16b we see that this initially very weak perturbation dramatically builds up and develops into a density wave of over 10% density contrast. For a pipe of same width but half the length, i.e. a different aspect ratio the wave has a less pronounced profile. This dependence on the aspect ratio is not to be confounded with finite size effects.

Triggering the density wave by two spatially separated perturbations, rather than just a single one, one can convince oneself that the complex shape of the waves does not reflect the detailed way in which they were initiated. We also observe that there seems to be no characteristic wavelength: Fig. 16b shows that the waves have roughly the same shape and that their size scales with the dimension of the channel.

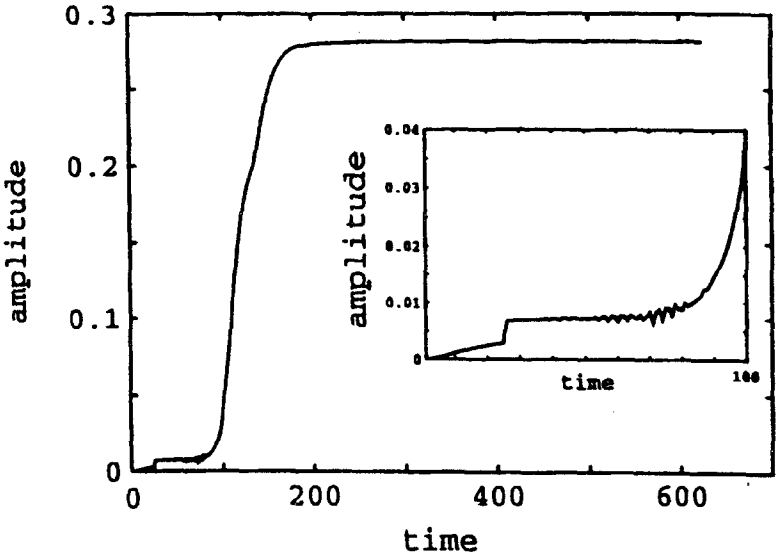

Fig. 17. Amplitude, i.e. difference between largest and smallest density, along the center of the pipe as a function of time measured in units of 100 iteration steps for $L = 256$ and otherwise the same parameters as in Fig. 16(right). The insert is a blow-up of the behavior at early times. (from Ref. [58])

Fig. 17 shows this amplitude as a function of time during 60,000 time steps. The insert shows the initial unstable phase leading to the rather drastic increase of the amplitude at the time 10,000. The first small increase in the density is due to the acceleration of the flow and can be understood from the velocity dependence in the pressure. The small jump at after 2500 time steps results from the perturbation. Before the instability is triggered at time 10,000, small oscillations

in the amplitude are observed. It was checked that the amplitude indeed has its steady state value at time 60,000 by running the simulations ten times longer. The complicated relaxation towards the fully developed density wave indicates that strong non-linear effects come into play rendering a linear stability analysis meaningless. It would be interesting to understand this behavior further.

A Lattice Gas model [95] can be formulated such as to include local dissipation of energy by introducing rest particles and special collision rules as done in Ref. [25]. Let us consider N particles located on the sites of a two dimensional triangular lattice which is L sites long and W sites wide. On each site there are seven Boolean variables i which are one or zero depending on whether there is a particle having velocity, $\boldsymbol{v}_i (i = 0, 1, 2, \cdots 6)$ or not. Here $\boldsymbol{v}_i (i = 1, 2, \cdots 6)$ are the nearest neighboring (NN) lattice vectors and $\boldsymbol{v}_0 = \mathbf{0}$ is the rest (zero velocity) state. So, each state can be either empty or occupied by a single particle and the number of particles per site has a maximal value of 7 and a minimal value of 0. The time evolution consists of a collision step and a propagation step. In the collision step particles change their velocities due to collisions and in the subsequent propagation step particles move in the directions of their velocities to the NN sites where they collide again except if there are rest particles. The system is updated in parallel. Only the specified collisions shown in Fig.18 can deviate the trajectories of particles. All collisions conserve mass and momentum.

For two- and three body collisions, one has the probabilistic rules shown in Fig. 18a. The probability that a configuration may take place is shown next to the configuration. If the parameter p is nonzero, energy is dissipated during the collision.

Two moving particles colliding with a rest particle from opposite directions can stop each other in accordance with momentum conservation. But on each site only one rest particle is allowed. Therefore, the two particles stay at rest on the NN sites where they originally came from. However, on these sites already other rest particles may exist. To make things simple, one can still use the on–site collision as defined and temporarily allow more than one rest particle on a site during the collision. Immediately after the collision, the extra rest particles randomly hop to NN sites until they find a suitable site with no rest particle already sitting there. This is one way to incorporate the existence of a maximum density. Another possibility which is in fact easier to implement on parallel computers consists of introducing also rest particles on bonds [26]. The collision rules with rest particles are shown in Fig. 18b.

The driving force of the flow is gravity. One simply incorporates its effect by giving with probability g to a rest particle a velocity along the direction of gravity and to any moving particle a change in velocity by a unit vector along gravity, if the resulting state is empty. (see Fig. 18c).

The sites at the walls of the system only have two directions into which the particles can move. So, a particle colliding with the wall from one direction can be bounced back with probability b and specularly reflected into the other direction with probability $1 - b$ as seen in Fig 18d. If $b = 0$, the walls are smooth (perfect no-slip condition). Otherwise, the walls have some roughness.

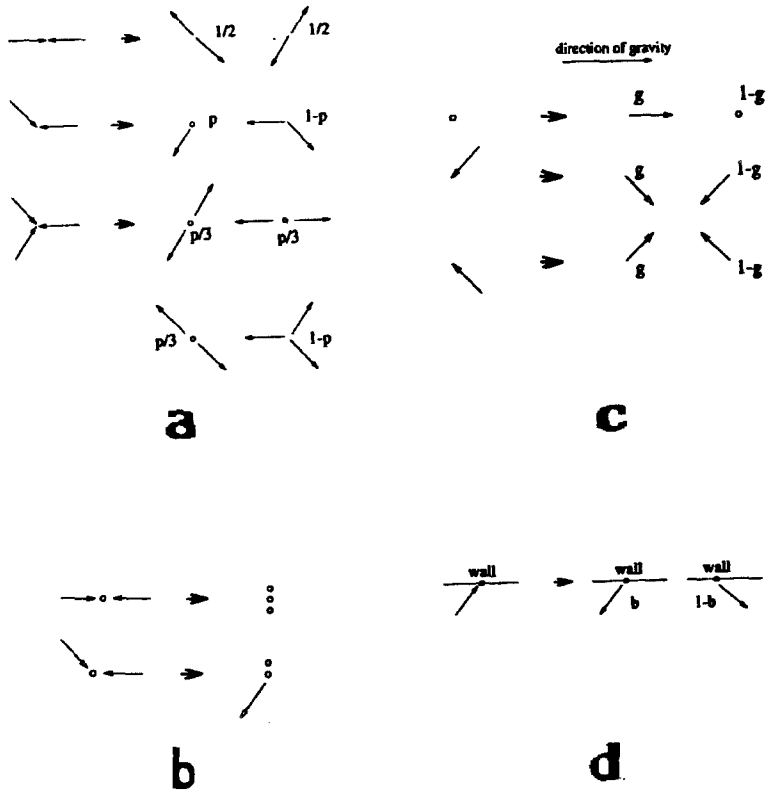

Fig. 18. (a) Probabilistic collision rules of the Lattice Gas of Ref. [25] (a) for two- and three body collisions, (b) for moving particles with a rest particle, (c) for gravity and (d) for a moving particle colliding with the wall. Thin arrows represent moving particles and small circles stand for rest particles. The number next to a configuration is the probability that the configuration takes place. Immediately after the collision, excessive rest particles on a site will randomly hop to the nearest neighboring sites until they find a suitable site with no rest particle already there.

Let us first consider a system with periodic boundary conditions in the direction of gravity. The initial configuration of the system is set to be random in the sense that every state (except the rest state) of each site is randomly occupied according to a preassigned average density ρ. Fig. 19 shows the time evolution of the density in the pipe during the early stage for $p = 0.1, g = 0.5, b = 0.5$. Here the system has length $L = 2200$ and width $W = 11$ with average density $\rho = 1.0$ The pipe was divided along the vertical direction into 220 bins with equal length of 10 and the number n_j of particles in the jth bin is counted. In Fig. 19 we

plot n_i in the ith bin by a grayscale which is a linear in n_i. The n_i at a given time are plotted from bottom to top while the densities at different time steps are plotted from left to right as time increases. Gravity is from bottom to top (usually it is plotted in the opposite direction). We see that initially the density is rather uniform and gradually regions of high density are being formed out of the homogeneous system. A high density region may also die out and two high density regions may merge to form a single one.

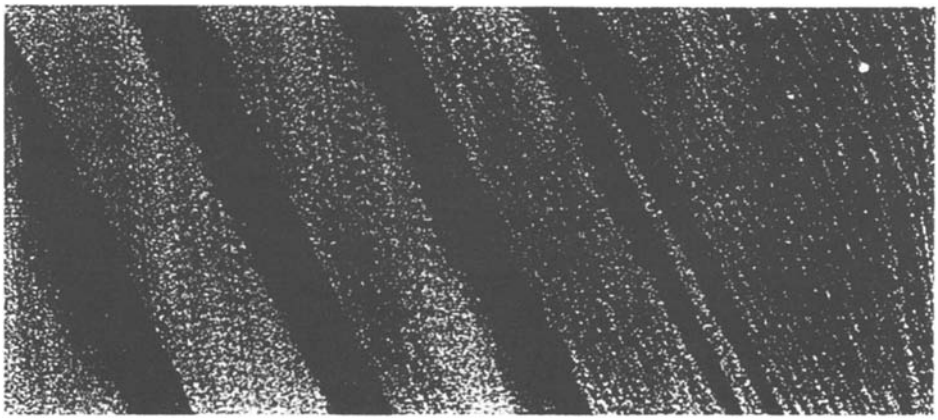

Fig. 19. Time evolution of the density $n_j\{j = 1, 2, \cdots 220\}$ divided in 220 bins along the pipe of $L = 2200$, $W = 11$ and $\rho = 1.0$. Densities at a given time are plotted from bottom to top (direction of gravity) while densities at different time steps are plotted from left to right (direction of time). Every 80 time steps are shown during 40,000 time steps. The grayscale of each bin is a linear function of n_i. Darker regions correspond to higher densities (from Ref. [25]).

To obtain the shape of the density waves one can record the density field in steady state at each time step and shift their spatial coordinates such that they overlap each other maximally. Since the density wave travels along the pipe, this shifted distance gives the average velocity. The maximal overlap rule can be applied hierarchically to obtain a clearer shape of the density wave. 64 simulation runs are then averaged to give the final density profiles which are presented in Fig.20. We notice that the density wave has a non–symmetric shape and its wave front is sharper than the backside of the wave. The width of the wave scales with the system length (almost linearly) and the amplitude of the wave only increases a little bit as the system length increases. Note the similarities to the profiles obtained with the LBG in Fig. 16.

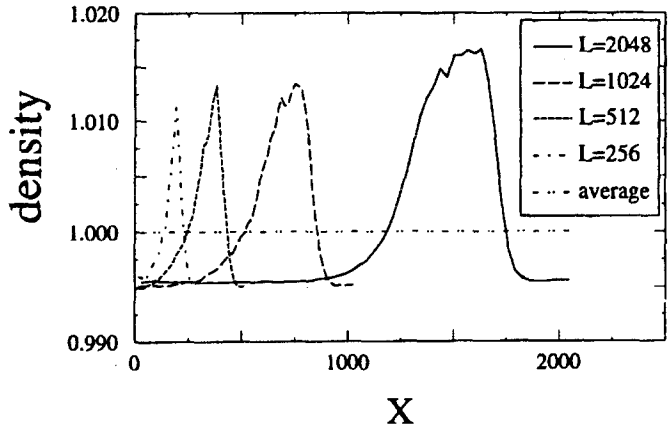

Fig. 20. Density as a function of position X along the pipe for various lengths L. The average has been made in the perpendicular direction. The model parameters are $\rho = 1.0$, $p = 0.1$, $g = 0.5$, $b = 0.5$ and $W = 11$ (from Ref. [25]).

To characterize the density fluctuations in a certain region with time, let us calculate their power spectra. The simulation is performed for very long time to obtain good statistics. One first subtracts the mean value from the data to remove the peak at $f = 0$ in the power spectra and calculates the spectra using a standard FFT routine. The power is the square of the amplitude of the Fourier Transformation of the time series. One representative power spectrum is shown in Fig. 21 for systems with $g = 0.5, b = 0.5, \rho = 1.0$ and $p = 0.8$. We observe a sharp peak due to the contribution of the density wave observed in Fig. 19. The frequency of this peak corresponds to a wave velocity of Lf/T_0 where L is the pipe length and T_0 is the time interval between two recordings (here $T_0 = 10$ time steps). The velocity measured in this way coincides with the direct measurement in real space. Apart from this peak one sees a background having a power law behavior where the spectrum falls off as $1/f^{\alpha}$. The exponent α is found to be around 1.33 in Fig. 21.

Both dissipation and the roughness of walls are necessary conditions for the presence of travelling density waves. If either $p = 0$ or $b = 0$ the spectrum has white noise. Neither the exponent of the power-law decay nor the velocity of the density wave do depend on dissipation p within the error bars. In fact, using a Kolmogorov–Obukhov approach revised for space–intermittent systems, Bershadskii [97] proposed that the exponent $\alpha = 1.33$ found for this model [25] might be a universal value of 4/3 for scalar fluctuations convected by stochastic velocity fields in dissipative systems. Our numerical results for the present LGA model show that the exponent does neither change with b nor with g but the average density ρ does affect the exponent. For very low density ($\rho \leq 0.8$) the exponent is zero, i.e. the density fluctuation in the pipe is just white noise since the interaction among the particles is so weak that no collective motion can

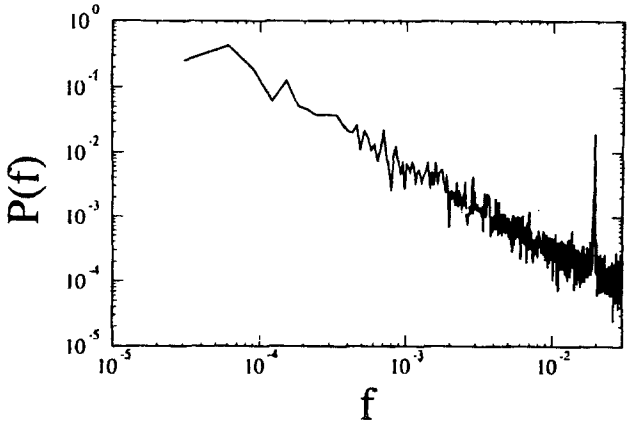

Fig. 21. Power spectrum $P(f)$ of the time series of the density fluctuation inside a region in a pipe of length L=220 and width W=11. The model parameters are $p = 0.8$, $b = 0.5$, $g = 0.5$, $\rho = 1.0$. The time series of the density fluctuation were recorded every 10 time steps (from Ref. [25]).

be formed. For average densities above 1.0, the exponent increases with ρ and becomes $\alpha \approx 1.86$ for $\rho = 2.0$. Beyond $\rho = 1.0$ the model cannot be taken very seriously anymore since when the number of rest particles exceeds the total number of sites there is an upper limit on the dissipation rate p that the system can bear.

From the experimental point of view, open boundary conditions are more realistic than the periodic boundary condition. Let us consider an open pipe which is initially empty. Particles are then injected from the upper boundary by a constant rate I and leave the system at the lower boundary without coming back. The injection rate is defined as follows. On each site of the upper boundary one considers the states with velocities pointing into the system. If such a state is not occupied, it can be filled with probability I. A time–evolution of the density in the pipe is shown in Fig. 22. Densities at a given time are plotted from bottom to top while densities at different time are plotted from left to right. Gravity acts from bottom to top. From this plot we observe that high density regions can also be formed in open systems. They travel along the pipe until they leave the system from the lower border or they may die out during their propagation. There are also more than one high density region at one time, in contrast to what we observed in Fig. 19 in periodic systems. It seems that all the density waves in Fig. 22 travel with a constant velocity.

The density fluctuations have been measured [25] in a bin very close to the bottom of the pipe. Its power spectrum is found to follow $1/f$ noise only around a critical injection rate $I_c = 0.52$ and white noise otherwise. Fig. 23 shows three power spectra for different injection rates, $I = I_c$, $I < I_c$ and $I > I_c$. The power spectrum for $I = I_c$ falls off with a slope close to -1 in the log–log plot. The

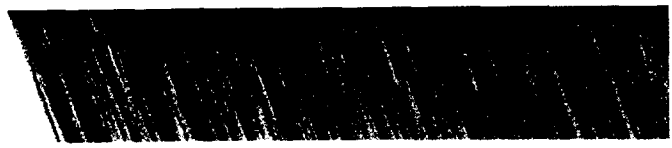

Fig. 22. Time evolution of the density $n_j\{j = 1, 2, \cdots 100\}$ in a pipe of $L = 1000$, $W = 5$ and $I = 0.5$. Other model parameters are $p = 0.5$, $b = 0.5$, $g = 0.2$. Densities at a given time are plotted from bottom to top (direction of gravity) while densities at different time steps are plotted from left to right (direction of time). Time goes from 0 to 40,000 time steps. The gray scale of each bin is a linear function of n_i. Darker regions correspond to higher densities (from Ref. [25]).

exponent α for the power spectra $1/f^{\alpha}$ is everywhere zero except around I_c. It seems that the power spectrum only has $1/f$ noise at the critical point. The critical injection rate is found to be independent on the model parameters and the system size. In fact one finds that for $I > I_c$ the system is clogging while for $I < I_c$ particles no clogging occurs. It seems that I_c is the maximal injection rate that the system can sustain without clogging.

9. A Thermodynamic Approach to Granular Media

Subjected to an external forces granular materials locally perform rather statistical motions due to their mutual collisions. For example on the loudspeaker the individual grains chaotically jump up and down forming a gas-like cloud of colliding particles. Also inside a shear-cell [15, 40, 98] or flowing down an inclined chute [41, 84] in addition to a laminar flow with a well defined (average) velocity profile one has Brownian-like motion of the particles perpendicular to the flow direction.

The above observations have inspired several authors to use thermodynamic concepts to describe granular media. On one hand a "granular temperature" T_{gr} has been defined [40, 99, 100] as $T_{gr} = \langle \boldsymbol{v}^2 \rangle - \langle \boldsymbol{v} \rangle^2$, i.e. proportional to the kinetic energy surplus with respect to the global motion. Strictly speaking this definition is thermodynamically justified if an equipartition theorem exists which is not the case for granular particles since they dissipate energy at collisions. On the other hand, Edwards and collaborators [23] have put forward another idea: Based on

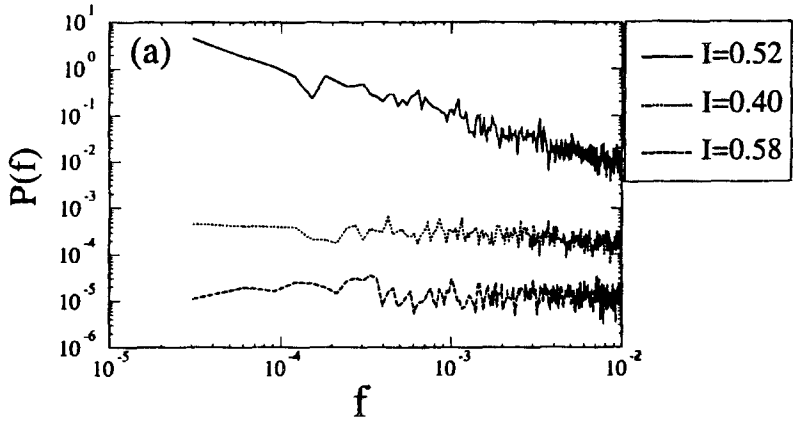

Fig. 23. Three typical power spectra for different injection rates I, $I = I_c = 0.52$ (top left), $I < I_c$ (top right), $I > I_c$ (bottom). The model parameters are $p = 0.5$, $b = 0.5$ and $g = 0.5$. The two lower curves have been shifted vertically for clarity (from Ref. [25]).

the important observation that granular materials do not conserve energy they proposed to consider the volume V to replace the internal energy in the usual thermodynamic formalism and define a temperature-like quantity $X = \partial V/\partial S$ which they called "compactivity". Although formally intact, this formalism is not easy to justify since in many real situations like on the vibrating table or on an inclined plane, the volume is not well limited at large heights. While Edwards's approach seems intuitively correct for dense packings and the definition of T_{gr} reasonable in the limit of strong internal motions or weak dissipation they fail in the corresponding opposite limit.

Let us present in the following a thermodynamic approach to granular materials [21] founded on similar principles as equilibrium thermodynamics which incorporates at least partially the intuitive pictures of previous work: We shall consider subsystems sufficiently small to have no velocity or density gradients and for which the energy flux into them is such that energy dissipation is homogeneous. Energy conservation implies that $\Delta I = \Delta E_{int} + \Delta D$ where ΔD is the energy dissipated in a given time and ΔI is the energy that was pumped into the system while ΔD was dissipated in order to maintain a steady state. The internal energy E_{int} is like in traditional thermodynamics the sum of kinetic and potential energy of all the degrees of freedom of the grains as elastic bodies (translation, rotation, elasticity, etc). One can now treat the excess dissipated energy $\Delta \mathcal{D} = \Delta D - \Delta I$ in a similar way as the heat in usual thermodynamics. Since the dissipated energy is proportional to the sum of normal forces f_n^i that push the particles together during collision i one can express changes in $\mathcal{D}$ as $\delta \mathcal{D} = \wp \delta C$ where $\wp$ is an internal pressure acting at collisions that we can define as $\wp = \rho \langle f_n^i / A_i \rangle$ where A_i is the area of contact of collision i and the average is

performed over all collisions. We define the density ρ of collisions as the number of collisions per unit volume and unit time. The extensive conjugate quantity C has a geometrical interpretation and plays the role of a potential. It should in fact be proportional [21] to the overlap volume V_{ov} that one has for technical reasons in MD simulations which can be defined more precisely as the excluded volume that would arise if the centers of mass of the particles follow the real trajectories but one does not take into account the elasto-plastic deformation. The "equilibrium" - which is in fact a steady state driven by the energy flux - can be defined as the ensemble *minimizing* C and one can *postulate* in analogy to the second law of thermodynamics that C should decrease for any change of state at constant internal energy E_{int}: $\Delta C \leq 0$ driven by the elastic repulsion between colliding (overlapping) grains.

As in usual thermodynamics one can now work in different ensembles. Naturally one would work at fixed $\wp$ (granular ensemble) in which a granular potential G_r can be defined as $G_r = E_{int} + \wp C$ and where at constant $\wp$ the equilibrium is given by the minimum of G_r. The response function κ defined as $\kappa = \frac{\partial \mathcal{D}}{\partial \wp} = \wp \frac{\partial C}{\partial \wp}$ measures how much more energy can be dissipated if $\wp$ is increased. On top of the granular ensemble one can build up the traditional body of thermodynamics as if the grains were a gas of particles interacting elastically. One can fix or free the number N of particles, define a "granular" temperature T_g and entropy S or impose to the system either an external volume V or an external pressure p. Special for granular media is that one could also impose an external shear τ or the dilatancy V_d [14, 15].

Considering a "state" given by the positions, orientations, linear and angular velocities of the grains as rigid bodies the entropy is well-defined as noted already in Ref. [23]. A reasonable definition for a "granular" temperature T_g would then be: $T_g = (\partial G_r / \partial S)_\wp$ which is, in fact, similar to the one defined previously [40, 99, 100] Experimentally $\wp$ and T_g are independent control parameters of the system: T_g is essentially driven by the amount ΔI of energy that is fed into the system per unit time. $\frac{\wp}{T_g}$ depends mainly on the density of collisions and can therefore increase by fragmenting the grains into smaller pieces. (Note that when a given grain is split into eight pieces, the cross section of each individual piece decreases by a factor four, so that $\wp$ will increase by two.)

10. Sound Propagation in Granular Assemblies

Recent experimental work shows that sound propagation in sand exhibits very complex behavior. Liu and Nagel [13] reported fluctuations in the acceleration-amplitudes measured at several points in the system. The spectrum of the time evolution of these amplitudes revealed a power law. They also measured the frequency response for their systems. The frequency response seems to be characteristic for the system, a slight rearrangement of the beads produces a completely different behavior. Leibig [101] calculated the frequency response for a system consisting of spherical particles interacting via linear springs on a square lattice. These numerical results are in agreement with the experimental ones [13].

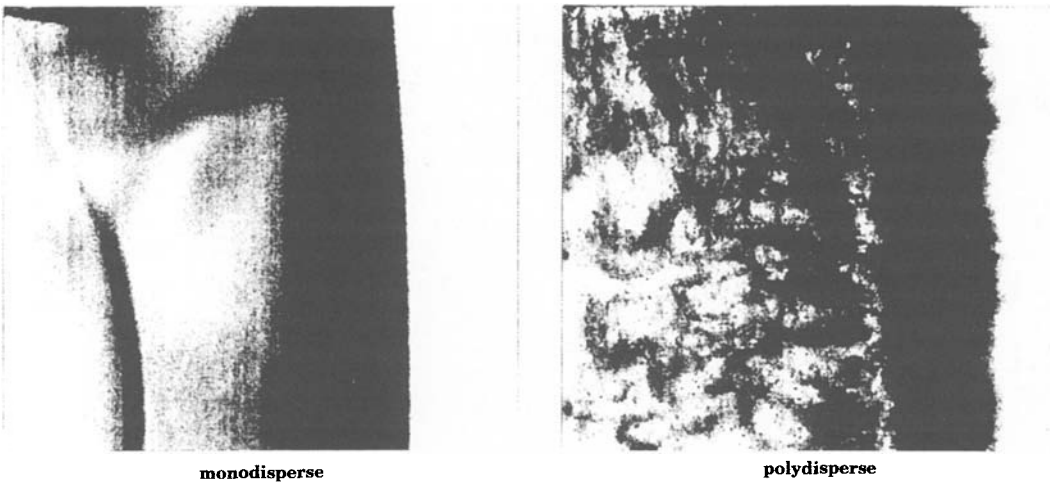

Fig. 24. Wave produced by a single compressional pulse of amplitude 0.01 d on the left wall. The grey scales code the kinetic energy of the particles. The left figure shows the monodisperse case and the right figure the polydisperse case. Note the secondary wave front clearly seen in the monodisperse case travelling (due to its lower amplitude) much slower behind the primary wave front (from Ref. [64]).

There have been predictions about the depth dependence of the sound velocity. Goddard made calculations [61] showing that the sound velocity v_c depends on pressure p like $v_c \propto p^{\frac{1}{6}}$ if the elastic interaction is Hertz's contact law. For high pressures this relation has been verified experimentally (cited in Ref. [61]). For low pressures, however, $v_c \propto p^{\frac{1}{4}}$ has been found experimentally. Both cases imply that the wave velocity approaches zero near the surface ($p = 0$), so that a vertical wave front will bend up, becoming increasingly horizontal which is known as the "mirage effect" [2, 13].

Melin [64] studied a two dimensional packing of grains confined within a rectangular box under gravity. The centers of the particles are situated on a triangular lattice. A sufficiently small perturbation (e.g. e weak polydispersity or a small vibration) can maintain the topology of this packing over regions much larger than the size of the container. So, since the neighbors are fixed throughout the entire simulation the time consuming part of determining the possible interaction partners can be avoided. This triangular lattice can be easily mapped onto a square lattice.

Melin [64] considers a system consisting of $256 * 256$ monodisperse spheres under gravity and puts on the left wall a step shaped excitation, i.e. all spheres at this wall are instantaneously moved a small distance to the right. On the

left part of Fig. 24 one can indeed recognize a rather weak dependence of the propagation velocity on depth. It is clear see that the relation $v_c \propto h^{\frac{1}{6}}$ cannot be valid in this case, because the wave near the surface has travelled a considerable distance. The reason for this behavior is that at the surface the particles touch each other and will exert some force on each other for any small perturbation.

This behavior can be quantified by measuring the position of the wavefront for every time step which can be chosen as the position of the particles which having the largest total energy at a given height. As one can clearly see in Fig. 25 the anticipated depth dependence of $v_c \propto h^{\frac{1}{6}}$ does not hold true for the simulated cases. The depth dependence becomes stronger with gravity. Moreover the propagation velocity of the wave front depends very much upon the amplitude of the initial excitation. Only for high amplitudes the depth dependence of the sound velocity becomes amplitude independent.

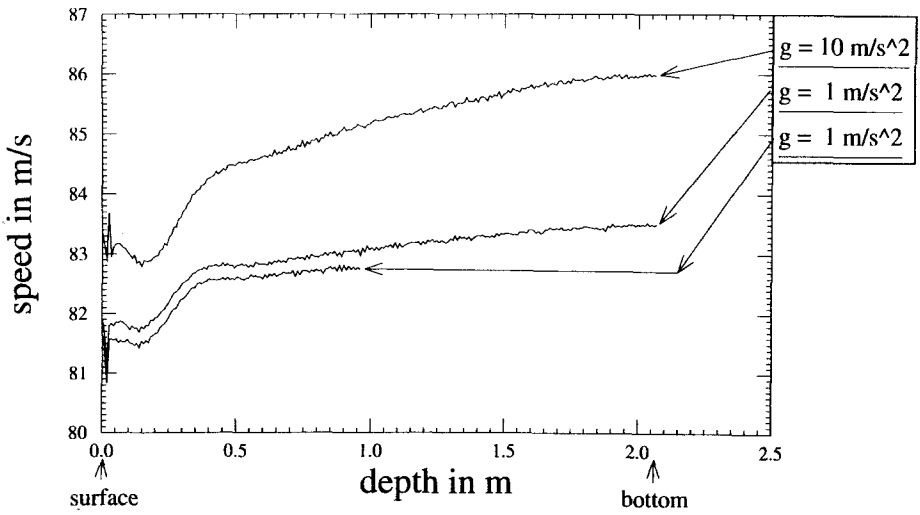

Fig. 25. Depth dependence of the sound velocity for two different values of gravity approximately 7.8 msec after the pulse. The third curve is for a system of only 256∗128 particles (i.e. half the height). It shows, that the boundary at the bottom only has a small effect. For better visualization this last curve has been shifted downwards by 0.25 m/sec. (from Ref. [64]).

It is interesting to note that the wave speed decreases with time. The explanation for this can be found in Fig. 24 where one can see that although the wavefront is very sharp the particles in the region behind the wavefront still have very much kinetic energy left. This means that the total energy in the wavefront decreases with time since some of energy is lost in the region it has traversed. Some of the kinetic energy is also lost due to its dissipation.

Introducing a polydispersity of $\Delta A_{max} = \pm 0.01 A$ where $A = d^2$ smears the wave front out but otherwise no qualitative difference in the general behavior is visible (see right part of Fig. 24). The reason for this can be seen in Fig. 26.

Due to the polydispersity some of the horizontal bonds are already closed in the equilibrated state. Any excitation will travel faster along these closed bonds.

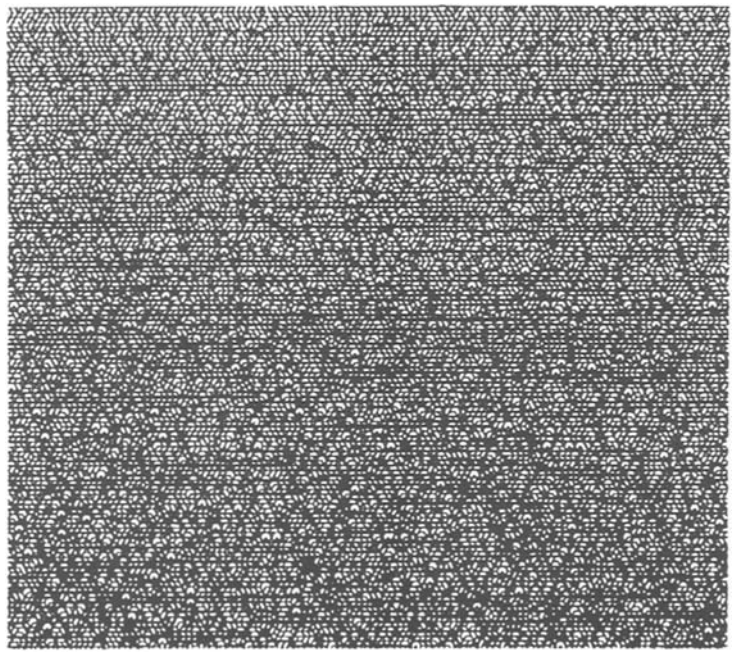

Fig. 26. Contact network for an equilibrated 256∗256 packing of spheres, the thickness of the lines is a measure for the stresses in the bonds. The particles have a polydispersity of 1% in the areas (from Ref. [64]).

Instead of looking at a single excitation, one can look at the behavior of a continuously excited system. Experimentally [13, 102] it is possible to measure the acceleration amplitudes and phases of a few test particles. The behavior turns out to be quite complex as seen in Fig. 27. The system has been driven sinusoidally at a frequency of 100Hz with an acceleration amplitude of $0.5g$. The particles forming the left wall are the sound source. Both figures have been taken 256 cycles (2.56 sec) after the beginning of the excitation. Fig. 27 shows the phases in x-direction for the monodisperse case.

One can see that the resulting patterns are far from regular. Note the very sharp phase shift on the right side of the system having an angle of 60°. These sharp phase shifts appear quite often. They are due to the confinement of the system in the rigid box [101].

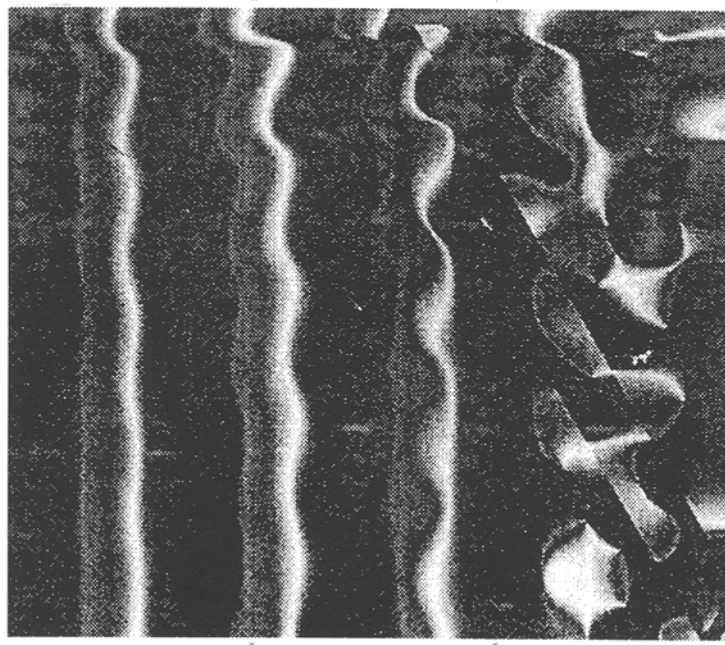

Fig. 27. The acceleration phases in x-direction for the monodisperse system 2.56 sec after starting the excitation (from Ref. [64]).

11. Plastic Deformation and Shear Bands in Dense Packings

The plastic yield criterion of granular material is quite different from that of metals because on one hand it linearly depends on pressure (Mohr-Coulomb) [103] and on the other hand because under shear a dilatation along an angle ψ is observed. The onset of plasticity is well described by a relation [103]:

$$\tau = c + \tan(\phi) \cdot \sigma_n \tag{11.1}$$

where τ and σ_n are the shear and the normal stresses and the material constants ϕ and c are the "friction angle" and the cohesion force, respectively. In general, the plasticity is "non-associate", i.e. the angle of dilatancy ψ under shear is different from ϕ.

Using an explicit Lagrangian technique similar to FLAC [104] an elasto-plastic rectangular medium was simulated in Ref. [65]. A compressive velocity in the horizontal direction was imposed. Besides the above mentioned material constants c, ϕ and ψ one can also change the elastic moduli or Lamé constants λ and μ. The simulations are performed on a grid which in its undeformed state is

a square lattice of unit lattice constant with an additional diagonal giving thus a triangulation. The numerical technique has an intrinsic time step Δt. Measured in these units a compressional velocity of 10^{-5} is imposed per grid element.

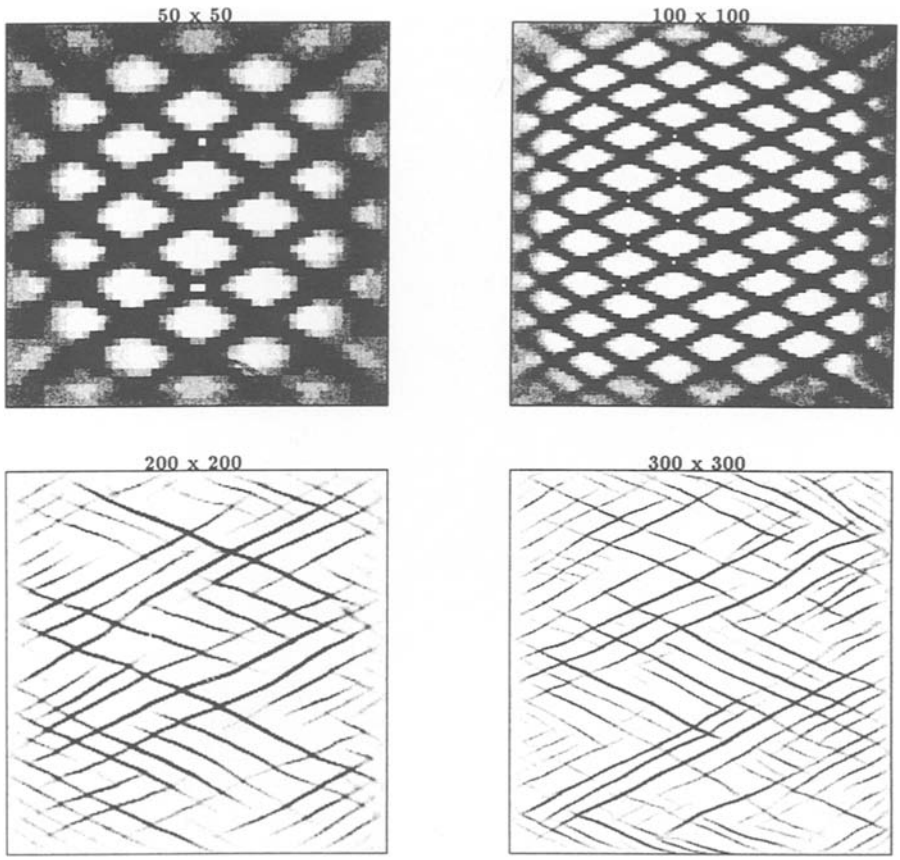

Fig. 28. Snapshot of the shear strain rate for systems of different size: (a) 50x50, (b) 100x100, (c) 200x200, (d) 300 x 300 for $\phi = 40$, $\psi = 0$, $c = 0$, $\lambda = \mu$, Poisson ratio $\nu = 0.25$ and $R = 10^{-9}$ (from Ref. [65]).

In Fig. 28 we see snapshots from the evolution of the systems with different mesh (lattice) sizes L but the same physical parameters. These results are shown after such a long time that the overall number of shear bands does not change with time (however the positions and activities of single shear zones is not constant).

The local changes of the second invariant of the strain rate: $e = \dot{\epsilon}_{II}$ determine the grey scale in Fig. 28. This means that the dark regions correspond to strong changes either in the direction or in the magnitude of the motion of the material. The white regions are elastic. We see that spontaneously shear bands are formed in which the plastic deformation occurs. These bands form an angle $45° - \phi/2 < \theta < (45° - \psi/2)$ with respect to the horizontal which is consistent with bifurcation theory [105, 106]. They have varying length and their position changes in time. Since our initial setup was completely homogeneous the random positions of the shear bands are due to minute effects in the round-off of the floating point numbers in the computer.

It has been observed that the pattern formed by the shear bands essentially only depends on the dimensionless parameter $R = pc/\mu V_{bc}$ where p is the confining pressure, c the velocity of sound, μ the Lamé constant and V_{bc} the externally imposed velocity of the boundary. This can be checked numerically by varying p, the elastic modulus and the size of the sample. With decreasing R shear bands are located closer to each other.

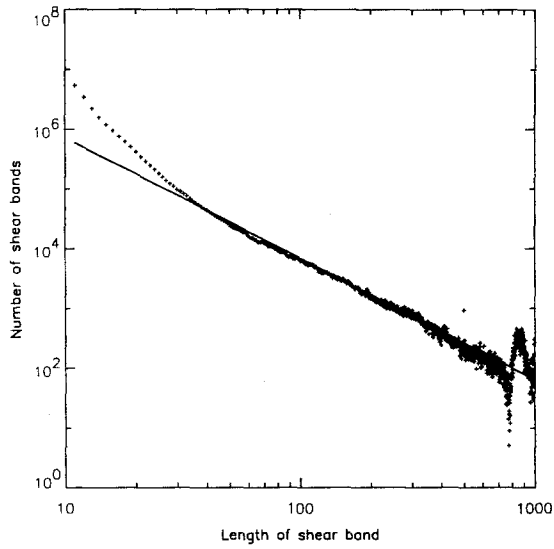

Fig. 29. Log-log plot of the length distribution for a system of size 300 x 300 for the same physical parameters as in Fig. 28. (from Ref. [65])

The scale invariance of the shear bands can be analyzed by changing the lattice size L or equivalently the resolution of the system. The geometrical fractal dimension of the shear band network is $d_0 = 1.82 \pm 0.1$ for $R = 10^{-9}$. The same result is obtained from the box-counting analysis of a single picture with the highest resolution [65].

The spontaneous appearance of a fractal set of shear bands starting out from a rather homogeneous situation suggests the existence of self-organized

criticality [54]. Each shear band might be seen as a single internal avalanche on which the system can release stresses through larger displacements. Let us also look at the distribution of the length of shear bands. Numerically the length of the bands can be obtained using a burning algorithm [107]. In Fig. 29 we see a log-log plot of this distribution. For lengths smaller than the width of the bands the data are not useful. After that we see a power-law decay with an exponent of $\tau = 2.1 \pm 0.2$. This value is in reasonable agreement with length distributions measured on sand [62].

There is some resemblance between fracture of rocks and shear bands in granular media. It is, however, important to point out a crucial difference between the two: for cracks the most stressed regions are at the tips while the shear bands have their strongest strain rates in the center.

12. Discussion

With a rather simple description of a granular medium as an ensemble of inelastic spherical particles with shear friction we have shown that many interesting rheological properties can be reproduced. Various types of convection can occur on a vibrating plate which are strongly influenced by hindrances on the wall. Density waves appear during the flow through a pipe which can be explained as a consequence of dissipation: Due to the inelastic collisions between particles (also cars) an instability [91, 92] tends to form clusters of high density (dark horizontal stripes in Fig. 12). These clusters self-organize into a critical state giving a power law spectrum. As in classical traffic models the density dependence of the flux generates kinematic waves (dark tilted lines in Fig. 12). The density dependence of the viscosity as predicted by kinetic gas theory builds up waves of low density (light horizontal lines in Fig. 12). We see that simply introducing dissipation to a gas of particles produces several phenomena, that occur simultaneously in granular materials.

It is not always straightforward to determine the material constants corresponding to some parameters of the model, like γ_n and γ_s, and so a quantitative comparison with experiments in many cases still involves fitting some parameters. More realistic models including static and dynamic friction, rotations of particles, variations in the particle shapes, etc increase the number of parameters but are needed to establish a closer contact to reality. The most important restriction of the simulations presented here is that most have been performed in two dimensions. Three dimensional simulations must also be performed since many phenomena seem to be due to steric effects. The technique we presented can of course also be applied to three dimensions. It is just the available computer time that limits at present our possibilities to extend simulations to three dimensional systems of numerically reliable sizes.

The analogy of molecular systems for which Molecular Dynamics simulations were originally conceived gave us the incentive to describe within a thermodynamic formalism the fluctuations arising from the constant flux and dissipation

of energy that drives a granular material's kinematic behavior. By separating the dissipative degree's of freedom (friction and plasticity) from the conservative ones (translation, rotation, elasticity) we define a "granular ensemble" coupled to a "dissipate bath" which is in fact the one in which experimental and numerical measurements are usually performed.

When the density of the granular medium exceeds the characteristic Reynolds dilatancy it behaves like a solid but retains very particular properties. One is the non-linear acoustics due to the complicated network on which the stresses are transmitted and another is the Hertzian contact law. As a consequence the sound velocity depends on pressure and amplitude and one finds secondary waves of lower velocity. Another effect is the non-associated plasticity due to the local effects of dilatancy during large scale deformations. Its consequence is the localization of the shear on planes which at least within a certain range form a fractal network.

I thank E. Flekkøy, J. Gallas, J. Lee, S. Melin, K. Nagel, G. Peng, A. Poliakov, T. Pöschel, G. Ristow and S. Sokołowski were my collaborators on the results presented in this course.

References

1. A. Hansen and D. Bideau (eds.) *Disorder and Granular Media* (North-Holland, Amsterdam, 1992)
2. H.M. Jaeger and S.R. Nagel, Science **255**, 1523 (1992) and S.R. Nagel, Rev. Mod. Phys. **64**, 321 (1992)
3. C.S. Campbell, Annu. Rev. Fluid Mech. **22**, 57 (1990)
4. A. Mehta, *Granular Matter* (Springer, Heidelberg, 1994)
5. J.C. Williams, Powder Techn. **15**, 245 (1976) and Fuel Soc. J. **14**, 29 (1963)
6. A. Rosato, K.J. Strandburg, F. Prinz and R.H. Swendsen Phys.Rev.Lett. **58**, 1038 (1987) and Powder Techn. **49**, 59 (1986); P. Devillard, J. Physique **51**, 369 (1990)
7. R. Jullien, P. Meakin and A. Pavlovitch, Phys. Rev. Lett. **69**, 640 (1992); R. Jullien and P. Meakin, Europhys. Lett. **22**, 523 (1993)
8. P.K. Haff and B.T. Werner, Powder Techn. **48**, 239 (1986)
9. M. Faraday, Phil. Trans. R. Soc. London **52**, 299 (1831)
10. P. Evesque and J. Rajchenbach, Phys. Rev. Lett. **62**, 44 (1989); C. R. Acad. Sci. Ser. 2, **307**, 1 (1988) and **307**, 223 (1988); C. Laroche, S. Douady and S. Fauve, J. de Physique **50**, 699 (1989); P. Evesque, J. Physique **51**, 697 (1990); J. Rajchenbach, Europhys. Lett. **16**, 149 (1991); E. Clément, J. Duran and J. Rajchenbach, Phys. Rev. Lett. **69**, 1189 (1992)
11. J. Walker, Sci. Am. **247**, 167 (1982); F. Dinkelacker, A. Hübler and E. Lüscher, Biol. Cybern. **56**, 51 (1987)
12. G.W. Baxter, R.P. Behringer, T.Fagert and G.A. Johnson, Phys. Rev. Lett. **62**, 2825 (1989)

13. C.-h. Lui and S.R. Jaeger, Phys. Rev. Lett. **68**, 2301 (1992)
14. O. Reynolds, Phil. Mag. Soc. **20**, 469 (1885)
15. Y.M. Bashir and J.D. Goddard, J. Rheol. **35**, 849 (1991)
16. E. Clément and J. Rajchenbach, Europhys. Lett. **16**, 133 (1991)
17. P. Evesque, E. Szmatula and J.-P. Denis, Europhys. Lett. **12**, 623 (1990); O. Zik and Stavans, Europhys. Lett. **16**, 255 (1991); O. Zik, J. Stavans and Y. Rabin, Europhys. Lett. **17**, 315 (1992)
18. G. Rátkai, Powder Techn. **15**, 187 (1976)
19. H.K. Pak and R.P. Behringer, Phys. Rev. Lett. **71**, 1832 (1993); S. Douady, thèse de doctorat, Ecole Normale Supérieure de Lyon
20. S.B. Savage, J. Fluid Mech. **92**, 53 (1979); G.M. Homsy, R. Jackson and J.R. Grace, J. Fluid Mech. **236**, 477 (1992); S.B. Savage and K. Hutter, J. Fluid Mech. **199**, 177 (1989)
21. H.J. Herrmann, J. Physique II **3**, 427 (1993)
22. J.T. Jenkins and S.B. Savage, J. Fluid Mech. **130**, 186 (1983)
23. S.F. Edwards and R.B.S. Oakeshott, Physica A **157**, 1080 (1989); S.F. Edwards, J. Stat. Phys. **62**, 889 (1991); A. Mehta and S.F. Edwards, Physica A **157**, 1091 (1989)
24. G.W. Baxter and R.P. Behringer, Phys. Rev. A **42**, 1017 (1990), Physica D **51**, 465 (1991); D. Désérable and J. Martinez, in *Powder & Grains* ed. C. Thornton (Balkema, Rotterdam, 1993), p. 345
25. G. Peng and H.J. Herrmann, Phys. Rev. E **49**, R1796 (1994) and preprint HLRZ 11/94
26. A. Károly and J. Kertész, Proc. 6th Joint EPS-APS Int. Conf. of Phys. Comp., eds. R. Gruber and M. Tomassini (EPS, Geneva, 1994)
27. H. Caram and D.C. Hong, Phys. Rev. Lett. **67**, 828 (1991) and Mod. Phys. Lett. B **6**, 761 (1992)
28. O. Walton, in *Two Phase Flow*, ed. M. Roco (Butterworth-Heinemann, Boston, 1992), chapter 25
29. G. Ristow, Ann. Rev. Comp. Phys., ed. D. Stauffer (World Sci. Publ. Co., Singapore, 1994)
30. P.A. Cundall, Report AD/A - 001 602, U.S. Nat. Tech. Information Service, (Springfield, Va, 1974)
31. P.A. Cundall and O.D.L. Strack, Géotechnique **29**, 47 (1979)
32. R.J. Bathurst and L. Rothenburg, J. Appl. Mech. **55**, 17 (1988)
33. Y. Zhang and P.A. Cundall, Proc. Symp. on the Mech. of Particulate Media, 10th National Congress on Applied Mechanics (Austin, Tex, (1986); J.M. Ting and B.T. Corkum, Proc. 6th Int. Conf. Num. Meth. in Geomech., Int. Commission for Num. Meth. in Geomech. **1**, 305 (1988); R. Dobry and T.T. Ng, Proc. 1st U.S. Conf. on Discrete Element Meth., Nat. Sci. Found. (Washington, DC, 1989); J.A. Issa and R.B. Nelson, idem; P.J. Hassan, thesis Univ. of Toronto (1990)
34. M.R. Kuhn and J.R. Mitchell, Proc. 1st U.S. Conf. on Discrete Element Meth., Nat. Sci. Found. (Washington, DC, 1989)
35. L.J. Lorig and B.H.G. Brady, ISRM British Geotech. Soc. (Cambridge, 1984), p.105

36. R. Barbosa and J. Ghaboussi, Proc. Workshop on Const. Laws for the Anal. of Fill Retention Struct., Canada Oil and Gas Adm. (Ottawa, 1987); M. Grabinsky, thesis Univ. of Toronto (1989); J.M. Ting, B.T. Corkum, C.R. Kauffman and C. Greco, J. of Geotech. Eng., ASCE **115**, 379 (1989)
37. T. Pöschel and H.J. Herrmann, preprint HLRZ 28/94
38. G. Ristow, J. Physique I **2**, 649 (1992) and Int. J. Mod. Phys. C **3**, 1281 (1992)
39. D.C. Hong and J.A. McLennan, Physica A **187**, 159 (1992)
40. C.S. Campbell and C.E. Brennen, J. Fluid Mech. **151**, 167 (1985); P.A. Thompson and G.S. Grest, Phys. Rev. Lett. **67**, 1751 (1991); D.M. Hanes and D.L. Inman, J. Fluid Mech. **150**, 357 (1985); O.R. Walton and R.L. Braun, J. Rheol. **30**, 949 (1986); M. Hakuno, K. Iwashita and Y. Uchida, Proc 1st U.S. Conf. on Discrete Element Meth., Nat. Sci. Found. (Washington, DC, 1989);
41. T. Pöschel, J. Physique II **3**, 27 (1993)
42. M.P. Allen and D.J. Tildesley, *Computer Simulation of Liquids*, Oxford University Press, Oxford, 1987
43. D. Tildesley, in *Computational Physics*, edited by R.D. Kenway and G.S. Pawley, NATO Advanced Study Institute, Edinburgh University Press, 1987
44. J.A.C. Gallas, H.J. Herrmann and S. Sokołowski, Physica A, **189**, 437 (1992)
45. S. Luding, E. Clément, A. Blumen, J. Rajchenbach and J. Duran, Phys. Rev. E **49**, 1634 (1994); S. Luding, H.J. Herrmann and A. Blumen, preprint HLRZ 77/93
46. Y-h. Tagushi, Phys. Rev. Lett. **69**, 1367 (1992) and preprints
47. J.A.C. Gallas, H.J. Herrmann and S. Sokołowski, Phys. Rev. Lett., **69**, 1371 (1992)
48. J.A.C. Gallas, H.J. Herrmann and S. Sokołowski, J. Physique II, **2**, 1389 (1992)
49. O. Cutress and R.F. Pulfer, Powder Techn. **1**, 213 (1967)
50. A. Drescher, T.W. Cousens and P.L. Bransby, Geotechn. **28**, 27 (1978)
51. R.L. Michalowski, Powder Techn. **39**, 29 (1984); J.D. Athey, J.O. Cutress and RF. Pulfer Chem. Eng. Sci. **21**, 835 (66); P.M. Blair-Fish and P.L. Bransby, J. Eng. for Industry **95**, 17 (73); J. Lee, S.C. Cowin and J.S. Templeton, Trans. Soc. Rheol. **18**, 247 (74); K.L. Schick and A.A. Verveen, Nature **251**, 599 (1974)
52. T. Pöschel, J. Physique I **4**, 499 (1994)
53. G.W. Baxter, R. Leone and R.P. Behringer, Europhys. Lett. **21**, 569 (1993); G.W. Baxter, R. Leone, G.A. Johnson and R.P. Behringer, Eur. J. Mech., B/Fluids **10**, #2 - Suppl., 181 (1991); G.W. Baxter, PhD thesis
54. P. Bak, Tang and Wiesenfeld, Phys. Rev. Lett. **59**, 381 (1987)
55. G.A. Held, D.H. Solina, D.T. Keane, W.J. Horn and G. Grinstein, Phys. Rev. Lett. **65**, 1120 (1990)
56. G. Ristow and H.J. Herrmann, Phys. Rev. E **50**, R5 (1994)
57. K. Nagel and H.J. Herrmann, Physica A **199**, 254 (1993)
58. E. Flekkøy and H.J. Herrmann, Physica A **199**, 1 (1993)
59. G. Ristow and H.J. Herrmann, preprint HLRZ 29/94
60. Experiments made in Cargèse in 1988
61. J.D. Goddard, Proc. R. Soc. London A **430**, 105 (1990)

62. A. Sornette, P. Davy and D. Sornette, Phys. Rev. Lett. **65**, 2266 (1990)
63. J.W. Rudnicki and Rice J.R., J.Mech.Phys. Solids, **23**, 371 (1975)
64. S. Melin, Phys. Rev. E **49**, 2353 (1994) and IJMPC **4**, 1103 (1993)
65. A. Poliakov and H.J. Herrmann, to appear in GRL and Fractals
66. K.L. Johnson, *Contact Mechanics* (Cambridge Univ. Press, 1989)
67. L.D. Landau and E.M. Lifshitz, *Elasticity Theory* (Pergamon Press, Oxford, 1975)
68. J. Lee and H.J. Herrmann, J. Phys. A **26**, 373 (1993)
69. T. Pöschel and H.J. Herrmann, Physica A**198**, 441 (1993)
70. T. Pöschel and V. Buchholtz, Phys. Rev. Lett. **71**, 3963 (1993); V. Buchholtz and T. Pöschel, Physica A **202**, 390 (1994)
71. W. Form, G.A. Kohring, S. Melin, H. Puhl and H.J. Tillemans, preprint HLRZ 75/93 for Comp. Meth. in Appl. Mech. and Eng.
72. F. Cantelaube, Y.L. Duparcmeur, D. Bideau and G.H. Ristow, preprint for J. de Physique
73. H. Schmidt and I. Peschl, Fördern u. Heben **15**, 606 (1965)
74. K. Ahmad and I.J. Smalley, Powder Technol. **8**, 69 (1973)
75. J. Bridgewater, Powder Technol. **15**, 215 (1976)
76. R.L. Brown, J. Inst. Fuel **13**, 15 (1939)
77. J. Duran, J. Rajchenbach and E. Clément, Phys. Rev. Lett. **70**, 2431 (1993)
78. R. Jullien, P. Meakin and A. Pavlovitch, Phys. Rev. Lett. **70**, 2195 (1993)
79. J.B. Knight, H.M. Jaeger and S.R. Nagel, Phys.Rev. Lett. **70**, 3728 (1993); E.E. Ehrichs, H.M. Jaeger, G.S. Karczmar, J.B. Knight, V. Kuperman and S.R. Nagel, preprint
80. J.B. Knight, C.G. Fandrich, C.N. Lau, H.M. Jaeger, S.R. Nagel, preprint
81. J. Duran, T. Mazozi, E. Clément and J. Rajchenbach, preprint
82. J. Duran, private communication
83. J.A.C. Gallas, H.J. Herrmann, T. Pöschel and S. Sokołowski, preprint HLRZ 92/93
84. T.G. Drake , J. Geophys. Res. **95**, 8681 (1990)
85. S.B. Savage, in *Powders and Grains*, ed. C. Thornton, Birmingham, 1993
86. J. Schwedes, *Fließverhalten von Schüttgütern in Bunkern* (Verlag Chemie, Weinheim, 1968)
87. K. Nagel and M. Schreckenberg, J. Physique I **2**, 2221 (1992)
88. M.J. Lighthill and G.B. Whitham, Proc. Roy. Soc. A **229**, 281 and 317 (1955); M. Leibig, Phys. Rev. E **49**, 184 (1994)
89. T. Musha and H. Higuchi, Jap. J. Appl. Phys. **15**, 1271 (1976)
90. M. de Sousa Vieira, Phys. Rew. A **46**, 6288 (1992)
91. I. Goldhirsch and G. Zanetti, Phys. Rev. Lett. **70**, 1619 (1993)
92. S. Savage, J. Fluid Mech. **241**, 109 (1992)
93. P.K. Haff, J. Fluid Mech. **134**, 401 (1983)
94. J.T. Jenkins, Arch. Rat'l. Mech. Anal., **87**, 355 (1985)
95. U. Frisch, B. Hasslacher and Y. Pomeau, Phys. Rev. Lett. **56**, 1505 (1986)

96. R. Benzi, S. Succi and M. Vergassola, Phys. Rep. **222**, 145 (1992); G.R. McNamara and G. Zanetti, Phys. Rev. Lett. **61**, 2332 (1988)
97. A. Bershadskii, Physica A **210**, 386 (1994)
98. R.A. Bagnold, Proc. Roy. Soc. London A **295**, 219 (1966) H.M. Jaeger, C.-h. Liu, S.R. Nagel and T.A. Witten, Europhys. Lett. **11**, 619 (1990)
99. S. Ogawa, *Proc. of US-Japan Symp. on Continuum Mechanics and Statistical Approaches to the Mechanics of Granular Media*, eds. S.C. Cowin and M. Satake (Gakujutsu Bunken Fukyu-kai, 1978), p.208
100. J.T. Jenkins and S.B. Savage, J. Fluid Mech. **130**, 186 (1983); H.M. Jaeger, C.-h. Lui and S.R. Nagel, Phys. Rev. Lett. **62**, 40 (1989)
101. M. Leibig, Phys. Rev. E **49**, 1647 (1994)
102. C. Liu, S.R. Nagel, Phys. Rev. B **48**, 15646 (1993)
103. J.D. Byerlee, J. Geophys. Res. **73**, 4741 (1968)
104. P.A. Cundall, Ingenieur Archiv **58**, 148 (1989)
105. P.A. Vermeer, Géotechnique **40**, (1990) 223; P.A. Vermeer and R. de Borst, Heron, **29**, 1 (1984)
106. I. Vardoulakis, Int. J. Numer. Anal. Meth. Geomech. **4**, 103 (1980)
107. H.J. Herrmann, D.C. Hong and H.E. Stanley, J. Phys. A **17**, L261 (1984)